JOURNAL OF MATHEMATICAL SCIENCES AND MODELLING

ISSN: 2636-8692

VOLUME IV
ISSUE III

VOLUME IV ISSUE III
ISSN 2636-8692

December 2021
http://dergipark.gov.tr/jmsm

JOURNAL OF MATHEMATICAL SCIENCES AND MODELLING

Editors

Editor in Chief
Soley Ersoy
Department of Mathematics,
Faculty of Science and Arts, Sakarya University,
Sakarya-TURKEY
sersoy@sakarya.edu.tr

Editor in Chief
Mahmut Akyiğit
Department of Mathematics,
Faculty of Science and Arts, Sakarya University,
Sakarya-TURKEY
makyigit@sakarya.edu.tr

Editor in Chief
Merve İlkhan Kara
Department of Mathematics,
Faculty of Science and Arts, Düzce University,
Düzce-TURKEY
merveilkhan@duzce.edu.tr

Managing Editor
Fuat Usta
Department of Mathematics,
Faculty of Science and Arts, Düzce University,
Düzce-TURKEY
fuatusta@duzce.edu.tr

Editorial Board of Journal of Mathematical Sciences and Modelling

Murat Tosun
Sakarya University,
TURKEY

George D. Magoulas
University of London,
UNITED KINGDOM

Zafer Bekir Yazıcı
Recep Tayyip Erdoğan University,
TURKEY

James F. Peters
University of Manitoba,
CANADA

Florentin Smarandache
University of New Mexico,
USA

Emrah Evren Kara
Düzce University,
TURKEY

Mujahid Abbas
University of Pretoria,
SOUTH AFRICA

Dağıstan Şimşek
Konya Technical University,
TURKEY

Syed Abdul Mohiuddine
King Abdulaziz University,
SAUDI ARABIA

Ismat Beg
Lahor School of Economics,
PAKISTAN

Wei Gao
School of Information Science and Technology,
P. R. CHINA

Murat Kirişçi
İstanbul University-Cerrahpaşa,
TURKEY

F. G. Lupianez
Complutense University of Madrid,
SPAIN

Yadigar Şekerci Fırat
Amasya University,
TURKEY

Khrisnan Balasubramanian
Arizona State University,
USA

Hidayet Hüda Kösal
Sakarya University,
TURKEY

Tamer Uğur
Atatürk University,
TURKEY

Khursheed J. Ansari
King Khalid University,
SAUDI ARABIA

Language Editor
Tolga Aktürk
Yıldız Technical University,
TURKEY

Technical Editor
Pınar Zengin Alp
Düzce University,
TURKEY

Technical Editor
Zehra İşbilir
Düzce University,
TURKEY

Editorial Secretariat
Bahar Doğan Yazıcı,
Bilecik Şeyh Edebali University,
TURKEY

Contents

Journal of Mathematical Sciences and Modelling, 4 (3) (2021) 104-109
Research Article

Journal of Mathematical Sciences and Modelling

Journal Homepage: www.dergipark.gov.tr/jmsm
ISSN 2636-8692
DOI: http://dx.doi.org/10.33187/jmsm.986344

A Note on Gershgorin Discs in the Elliptic Plane

Arzu Sürekçi[1*], Hidayet Hüda Kösal[1] and Mehmet Ali Güngör[1]

[1]*Sakarya University, Faculty of Arts and Sciences, Department of Mathematics, 54187 Serdivan/Sakarya, Turkey*
[*]*Corresponding author*

Article Info

Keywords: *Elliptic complex matrix, Elliptic complex numbers, Elliptic valued polynomial, Gershgorin discs.*
2010 AMS: *14H52, 15A18.*
Received: *23 August 2021*
Accepted: *16 October 2021*
Available online: *29 December 2021*

Abstract

In this study, we derive Gershgorin discs of elliptic complex matrices in the elliptic plane. Also, we investigate the location of the zeros of an elliptic complex-valued polynomial with the help of Gershgorin discs of elliptic complex matrices. To prove the authenticity of our results and to distinguish them from existing ones, some illustrative examples are also given. Elliptic complex numbers are a generalized form of complex and so real numbers. Thus, the obtained results extend, generalize and complement some known Gershgorin discs results from the literature.

1. Introduction

The Gershgorin set that is composed of a union of discs, is a region that is inclusive of eigenvalues of matrices. This result is stated in the following theorem, where the deleted row sum R_i' of a complex matrix A with elements a_{ij} is defined as;

$$R_i' = \sum_{j=1,\, j\neq i}^{n} |a_{ij}|.$$

Theorem 1.1. *(Gershgorin's Theorem) All the eigenvalues of the $n \times n$ complex matrix A are located in the union of the discs n*

$$\bigcup_{i=1}^{n} \Gamma_i^R = \Gamma^R$$

where

$$\Gamma_i^R = \left\{ z \in C : \ |z - a_{ii}| \leq R'_i \right\}.$$

The Gershgorin set in matrix theory has important applications in modeling human faces, size reduction and data compression, signal and image processing-restoration, computational mathematics, some fields of pure and applied mathematics and so on [1]−[10]. With the rapid development of these fields, more and more researchers are interested in the Gershgorin set and have obtained many valuable results. For the Gershgorin set, they mainly consider real, complex and real quaternion matrices.

On the other hand, elliptic complex numbers are defined as

$$z = x + uy$$

where $x,\ y \in R$ and $u^2 = p < 0 \in R$. Since many physical systems have elliptical behaviors, elliptic complex number systems have many applications in science and technology, [11]−[18]. Thus, it is getting more and more necessary for us to further study the theoretical properties and numerical computations of elliptic complex numbers and their matrices.

In this study, we introduce concepts of the Gershgorin sets of the elliptic complex matrices and investigate the location of the zeros of an elliptic complex-valued polynomial with the help of this theory. To prove the authenticity of our results and to distinguish them from existing ones, some illustrative examples are also given. Elliptic numbers are a generalized form of complex and so real numbers. Thus, the obtained results extend, generalize and complement some known Gershgorin set results from the literature.

***Email addresses and ORCID numbers*: arzu.cihan3@ogr.sakarya.edu.tr , 0000-0003-2003-3507 (A. Sürekçi), hhkosal@sakarya.edu.tr, 0000-0002-4083-462X (H.H. Kösal), agungor@sakarya.edu.tr, 0000-0003-1863-3183 (M.A. Güngör)**

2. Algebraic Properties of Elliptic Complex Numbers

The set of elliptic complex numbers is denoted by

$$C_p = \left\{ z = x + uy : \ x, y \in R, \ u^2 = p < 0 \right\}.$$

For a elliptic complex number $z = x + uy \in C_p$, the real number $\mathrm{Re}(z) = x$ is called the real part of z and $\mathrm{Im}(z) = y$ is called the imaginary part of z.
The conjugate and norm of elliptic complex number $z = x + uy$ are defined as

$$\overline{z} = x - uy \ \text{ and } \ \|z\|_p = \sqrt{z\overline{z}} = \sqrt{x^2 - py^2},$$

respectively.
Addition, multiplication and scalar multiplication of the elliptic complex numbers $z_1 = x_1 + uy_1, \ z_2 = x_2 + uy_2 \in C_p$ are defined by

$$z_1 + z_2 = (x_1 + uy_1) + (x_2 + uy_2) = x_1 + x_2 + u(y_1 + y_2),$$

$$z_1 z_2 = (x_1 + uy_1)(x_2 + uy_2) = (x_1 x_2 + p y_1 y_2) + u(x_1 y_2 + x_2 y_1),$$

$$\lambda z_1 = \lambda (x_1 + uy_1) = \lambda x_1 + u\lambda y_1, \quad \lambda \in R,$$

respectively, [19].

Theorem 2.1. *C_p is 2D vector space over a field R according to addition and scalar multiplication, [20].*

Also, each elliptic complex number can be represented in a single form in an elliptic plane. In the elliptic plane, the distance between of the elliptic complex numbers $z_1 = (x_1, y_1)$ and $z_2 = (x_2, y_2)$ is defined as

$$\|z_1 - z_2\|_p = \sqrt{(x_1 - x_2)^2 - p(y_1 - y_2)^2},$$

[19].
Unit circles are defined by requiring $\|z\|_p = \sqrt{x^2 - py^2} = 1$ as in Figure 2.1 In special case $p = -1$, the elliptic plane corresponds to the Euclidean plane.

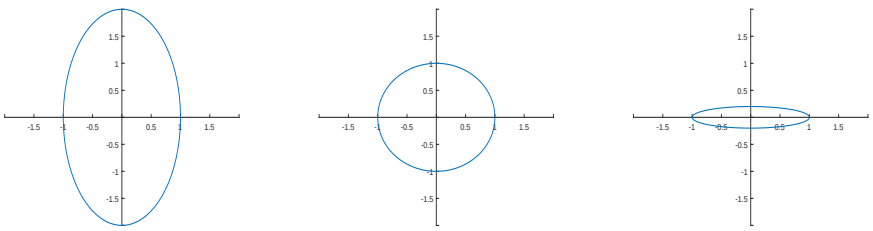

(a) **(b)** **(c)**

Figure 2.1: Unit circles in $C_{-0.5}, C_{-1}, C_{-5}$.

Definition 2.2. *Let $z = x + uy \in C_p$ be given. C_p is algebraically isomorphic to complex numbers*

$$C = \left\{ x + iy \mid x, \ y \in R \ \text{ and } i^2 = -1 \right\}$$

through the bijective map

$$\begin{aligned} &\alpha_p : C_p \to C \\ &z = x + uy \to \alpha_p(z) = x + i\sqrt{|p|}y, \end{aligned}$$

[19].

The fundamental theorem of algebra for complex-valued polynomials: Let us consider the polynomial f with real coefficient and degree $N > 0$. So, thanks to the polynomial f, two algebraic curves are defined by

$$\mathrm{Re}(f(z)) = 0 \quad \text{and} \quad \mathrm{Im}(f(z)) = 0.$$

Each of these two algebraic curves consists of different continuous branches and these curves intersect the circle $\|z\| = r$ at $2N$ points. In addition, the crossing points of these two algebraic curves remain within this circle. This shows that the polynomial f has at least one real root, [21].
Now let's give the fundamental theorem of algebra for complex numbers that Gauss proved given above for elliptic complex-valued polynomials.

Theorem 2.3. *A $n-th$ degree polynomial function with elliptic complex coefficients and elliptic complex-valued*

$$f_p(z)=\sum_{i=0}^{n}a_iz^i=z^n+a_{n-1}z^{n-1}+...+a_1z+a_0$$

has exactly n zeros in the set of the elliptic complex numbers, counting repeated zeros.

Proof. Let $z=x+uy\in C_p$ be given. Considering the Definition 2.2 we can express each elliptic complex number in terms of the complex number. Then we can take a complex number instead of an elliptic complex number using the equation $u=i\sqrt{|p|}$ and the equivalence $z=x+uy\equiv x+i\sqrt{|p|}y$ exists. Let $f_p(z)$ be the $n-th$ order monic polynomial with the elliptic complex-valued real coefficient

$$f_p(z)=z^N+c_{N-1}z^{N-1}+...+c_1z+c_0=z^N+\sum_{n=0}^{N-1}c_nz^n,$$

where $z=x+uy\in C_p$ and $c_0,c_1,...,c_{N-1}\in R$.
Considering the equation $z=x+uy\equiv x+i\sqrt{|p|}y$, the polynomial $f_p(z)$ becomes a monic polynomial with $n-th$ order complex-valued real coefficients. Therefore, according to the fundamental theorem of algebra for complex valued and complex coefficients, the polynomial f has at least one root. Let $z_0=x_0+iy_0$ be one root of $f_p(z)$. In this case, taking into account the equality $u=i\sqrt{|p|}$, the equality $z_0=x_0+\frac{u}{\sqrt{|p|}}y_0$ can be written and z_0 becomes a root of the polynomial f_p. As a result, every $n-th$ order monic polynomial with elliptic complex-valued and real coefficient has at least one root. □

This theorem is true for all polynomials with elliptic complex coefficients. To see why this is true, suppose the theorem holds for elliptic complex-valued polynomials with real coefficients, and let $f_p(z)=z^N+c_{N-1}z^{N-1}+...+c_1z+c_0$, be an elliptic complex valued polynomial with elliptic complex coefficients. Let $\overline{f_p}(z)=z^N+\overline{c_{N-1}}z^{N-1}+\ldots+\overline{c_0}$ be the polynomial whose coefficients are the elliptic conjugates of the coefficients of f, and let $g_p(z)=f_p(z)\overline{f_p}(z)=f_p(z)\overline{f_p(z)}$. Then g is a polynomial with real coefficients, so by assumption it has a root z_0. This means that $g_p(z_0)=f_p(z)\overline{f_p(\overline{z})}$, so either z_0 or $\overline{z_0}$ is a root of f.

Also, according to our theorem, the two curves $\mathrm{Re}\left(f_p(z)\right)=0$ and $\mathrm{Im}\left(f_p(z)\right)=0$ must intersect at some point in the interior of the elliptic disc. At this intersection point, the real and imaginary parts of $f_p(z)$ are both 0, so $f_p(z)=0$; in other words, the intersection point is a root of f.

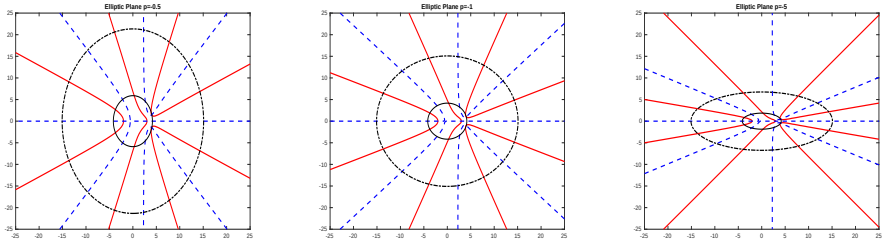

(a) **(b)** **(c)**

Figure 2.2: The solid red lines are the points where $\mathrm{Re}(f_p(z))=0$ and the dashed blue lines are the points where $\mathrm{Im}(f_p(z))=0$ in elliptic plane for the elliptic complex valued polynomial $f_p(z)=z^4-9z^3+19z^2+31z-102$. In here intersection points of algebraic curves $\mathrm{Re}(f_p(z))=0$ and $\mathrm{Im}(f_p(z))=0$ in elliptic plane are root of $f_p(z)$. Also, the large, solid ellipse is $|z|=r^*$, and the smaller, dotted ellipse is $|z|=r_0$.

The set $C_p^{m\times n}$ denotes all $m\times n$ type matrices with elliptic complex number entries. For $A=A_1+uA_2$, $B=B_1+uB_2\in C_p^{m\times n}$, $C=C_1+uC_2\in C_p^{n\times l}$ the ordinary matrix addition, scalar multiplication and multiplication are defined by

$$A+B=(A_1+uA_2)+(B_1+uB_2)=(A_1+B_1)+u(A_2+B_2)\in C_p^{m\times n},$$

$$\lambda A=\lambda(A_1+uA_2)=\lambda A_1+u(\lambda A_2)\in C_p^{m\times n}$$

and

$$AC=(A_1+uA_2)(C_1+uC_2)=(A_1C_2+pA_2C_2)+u(A_1C_2+A_1C_1)\in C_p^{m\times l},$$

respectively.

Theorem 2.4. *[22] Let A and B be elliptic complex matrices of appropriate sizes. Then the following are satisfied:*

1. $\left(A^{-1}\right)^{-1}=A$,
2. $(AB)^{-1}=B^{-1}A^{-1}$,
3. $\left(A^k\right)^{-1}=\left(A^{-1}\right)^k$, $k\in Z^+$,
4. $\left(A^T\right)^T=A$,
5. $(\lambda A)^T=\lambda A^T$,

6. $(AB)^T = B^T A^T$,
7. $\left(A^k\right)^T = \left(A^T\right)^k$, $k \in Z^+$,
8. $\overline{(\overline{A})} = A$, $(A^*)^* = A$,
9. $\overline{(A+B)} = \overline{A} + \overline{B}$, $(A+B)^* = A^* + B^*$,
10. $\overline{(AB)} = \overline{A}\,\overline{B}$, $(AB)^* = B^* A^*$.

Definition 2.5. *Let $A \in C_p^{n\times n}$, $\lambda \in C_p$. If there exists $0 \neq x \in C_p^{n\times 1}$ such that*

$$Ax = \lambda x$$

then λ is called a eigenvalues of A and x is called a eigenvector of A associate with λ. The set of eigenvalues of elliptic complex matrix A is defined as

$$\sigma_p(A) = \left\{\lambda \in C_p : Ax = \lambda x,\ \exists x \neq 0\right\}.$$

Theorem 2.6. *Elliptic complex matrix $A \in C_p^{n\times n}$ has exactly n elliptic eigenvalues.*

Proof. Since the characteristic polynomial $f_A(s) = \det(A - sI)$ of matrix $A \in C_p^{n\times n}$ will be an $n-th$ order polynomial, from the fundamental theorem of algebra for elliptic complex numbers, matrix A has at most n eigenvalues. □

Example 2.7. *Let find the eigenvalues of the elliptic complex matrix*

$$A = \begin{pmatrix} 1+u & 0 & 1 \\ 0 & u & 0 \\ 1 & 0 & 1-u \end{pmatrix} \in C_p^{3\times 3}.$$

Characteristic polynomial of the elliptic complex matrix A is $f_A(s) = \det(A - sI_{2\times 2}) = (s-u)(s^2 - 2s - p)$. Zeros of f_A are

$$s_1 = u, \quad s_2 = 1 + \sqrt{1-p}, \quad s_3 = 1 - \sqrt{1-p}.$$

These roots are also the eigenvalues of the matrix A. The eigenvalues of the matrix A according to the values p are given in the table below.

	λ_1	λ_2	λ_3
$p = -0.5$	1.7071	0.2929	u
$p = -1$	1	1	u
$p = -5$	$1 + 0.8944u$	$1 - 0.8944u$	u

Table 1: The eigenvalues of the matrix A according to the values p.

Theorem 2.8. *Each eigenvalue of the elliptic complex matrix $A \in C_p^{n\times n}$ is inside at least one of the ellipses $D_i(A)$ in the elliptic plane,*

$$D_i(A) = \left\{z : \|z - a_{ii}\|_p \leq R_i,\ 1 \leq i \leq n\right\}$$

in here $R_i = \sum_{j\neq i} \|a_{ij}\|_p$. In other words, all the eigenvalues of matrix A are in the region $D(A)$,

$$D(A) = \bigcup_{i=1}^{n} D_i(A).$$

Proof. Let's admit that λ is an eigenvalue of matrix A. In this case, there is a non-zero vector $x = (x_1, x_2, ..., x_n)^T \in C_p^{n\times 1}$ such that $Ax = \lambda x$. Let's say x_k is the largest component of x, so

$$\|x_k\|_p = \max\left\{\|x_i\|_p,\ 1 \leq i \leq n\right\} > 0$$

is. In this case

$$\sum_{j\neq k} a_{kj} x_j = (\lambda - a_{kk})$$

can be written from the equation $a_{k1}x_1 + a_{k2}x_2 + ... + a_{kn}x_n = \lambda x_k$. In the last equation, the norm of both sides of the equation is taken and if the triangle inequality is used,

$$\begin{aligned} \|\lambda - a_{kk}\|_p \|x_k\|_p &= \left\| \sum_{j\neq k} a_{kj} x_j \right\|_p \\ &\leq \sum_{j\neq k} \|a_{kj}\|_p \|x_j\|_p \\ &\leq \left(\sum_{j\neq k} \|a_{kj}\|_p \right) \|x_k\|_p \end{aligned}$$

is obtained. Here,

$$\|\lambda - a_{kk}\|_p \leq \sum_{j\neq k} \|a_{kj}\|_p$$

inequality is obtained.
If it is called

$$R_i = \sum_{j\neq i} \|a_{ij}\|_p = \|a_{i1}\|_p + \|a_{i2}\|_p + ... + \left\|a_{i(i-1)}\right\|_p + \left\|a_{i(i+1)}\right\|_p + ... + \|a_{in}\|_p \ \ (i = 1,2,3,...,n),$$

it is proved that each eigenvalue of the elliptic matrix $A \in C_p^{n\times n}$ is inside at least one of ellipses in the elliptic plane

$$D_i(A) = \left\{z : \|z - a_{ii}\|_p \leq R_i,\ 1 \leq i \leq n\right\}.$$

□

Example 2.9. *Let*

$$A = \begin{pmatrix} 4-3u & u & 2 & -2 \\ u & -1+u & 0 & 0 \\ 1+u & -u & 5+6u & 2u \\ 1 & -2u & 2u & -5-5u \end{pmatrix} \in C_p^{4\times 4}.$$

According to the Theorem 2.8 we have

$$R_1 = 4+\sqrt{-p},\ R_2 = \sqrt{-p},\ R_3 = \sqrt{1-p}+3\sqrt{-p} \text{ and } R_4 = 1+4\sqrt{-p}.$$

For elliptic complex matrix A there are Gershgorin disc:

$$\begin{aligned} D_1 &: (x-4)^2 - p(y+3)^2 \leq (4+\sqrt{-p})^2 \\ D_2 &: (x+1)^2 - p(y-1)^2 \leq (\sqrt{-p})^2 \\ D_3 &: (x-5)^2 - p(y-6)^2 \leq \left(\sqrt{1-p}+3\sqrt{-p}\right)^2 \\ D_4 &: (x+5)^2 - p(y+5)^2 \leq (1+4\sqrt{-p})^2. \end{aligned}$$

In the elliptic plane, regions of the eigenvalues of the matrix A according to the state of p are as shown in the lower graph.

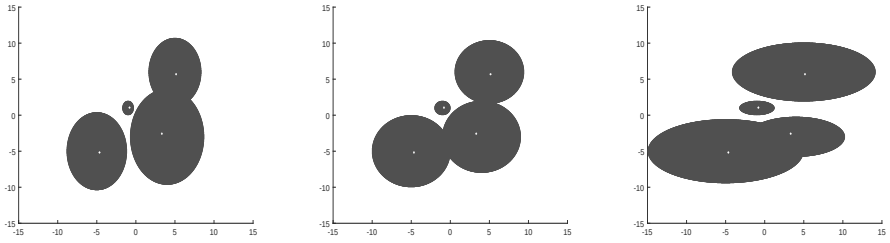

(a) **(b)** **(c)**

Figure 2.3: In elliptic plane Gershgorin discs for $p = -0.5, p = -1$ and $p = -5$, *respectively.*

Locate Zeros of Polynomials: Eigenvalue inclusion sets can be used to locate zeros of elliptic valued polynomials by using the polynomial's companion matrix, whose characteristic polynomial is the given polynomial, [23]−[28]. Thus, its eigenvalues are the zeros of the polynomial. The companion matrix of elliptic valued monic polynomial $f_p(z) = \sum_{i=0}^{n} a_i z^i = z^n + a_{n-1}z^{n-1} + ... + a_1 z + a_0$ is

$$C_p(f) = \begin{pmatrix} 0 & 0 & \cdots & 0 & -a_0 \\ 1 & 0 & \cdots & 0 & -a_1 \\ 0 & 1 & \cdots & 0 & -a_2 \\ \vdots & \vdots & \vdots & \vdots & \vdots \\ 0 & 0 & \cdots & 1 & -a_{n-1} \end{pmatrix}.$$

Figure 2.4 shows regions of the zeros of the elliptic valued polynomial $f_p(z) = z^4 - z^3 + 0.2z^2 - 0.1z + 2$ according to the state of p. The zeros are indicated by the white dots.

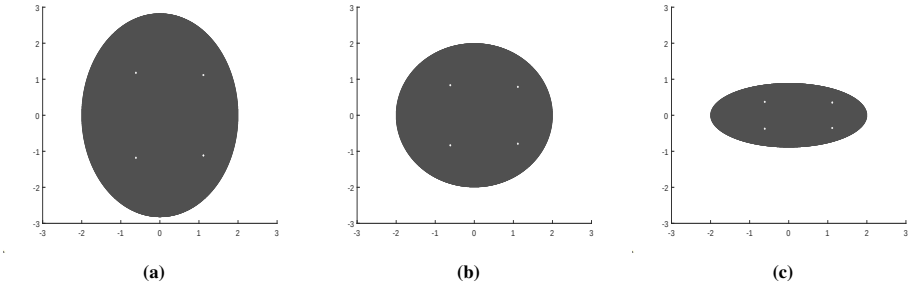

(a) **(b)** **(c)**

Figure 2.4: Regions of the zeros of the elliptic valued polynomial $f_p(z)$ for $p = -0.5$, $p = -1$ and $p = -5$, respectively.

3. Conclusions

In this study, we derive Gershgorin discs of elliptic complex matrices in the elliptic plane. Eigenvalues of matrices have important applications in modeling human faces, gene analysis, information retrieval and extraction, size reduction and data compression, signal and image processing-enhancement processes. The use of elliptic matrices in these application areas will enable the previously known definitions and theorems to be interpreted with a wider perspective, and by selecting the ideal space for the problems, great flexibility and efficiency will be brought to existing techniques.

References

[1] F.A. Aliev, V.B. Larin, *Optimization of linear control systems*, USA, CRC Press, 1998.
[2] D. Calvetti and L. Reichel, *Application of ADI iterative methods to the restoration of noisy images*, SIAM J. Matrix Anal. Appl., **17**(1) (1996), 165-186.
[3] L. Dieci, M.R. Osborne and R.D.Russel, *A Riccati transformation method for solving linear BVPs. I: Theoretical Aspects*, SIAM J. Numer. Anal., **25**(5) (1988), 1055-1073.
[4] W.H. Enright, *Improving the efficiency of matrix operations in the numerical solution of stiff ordinary differential equations*, ACM Trans. Math. Software, **4**(2) (1978), 127-136.
[5] M.A. Epton, *Methods for the solution of AXD - BXC = E and its applications in the numerical solution of implicit ordinary differential equations*, BIT Numer. Math., **20** (1980) 341-345.
[6] F.R. Gantmacher, *The theory of matrices*, New York, Chelsea Publishing Company, 1959.
[7] A. Jameson, *Solution of the equation $ax+xb=c$ by inversion of an $m\times m$ or $n\times n$ matrix*, SIAM J. Appl. Math., **16**(5) (1968), 1020-1023.
[8] E. Souza, *Controllability, observability and the solution of $ax-xb=c$*, Linear Algebra Appl., **39** (1981), 167-188.
[9] M. Dehghan and M. Hajarian, *Efficient iterative method for solving the second-order Sylvester matrix equation $EVF^2-AVF-CV=BW$*, IET Control Theory Appl., **3**(10) (2009), 1401-1408.
[10] A. Wu, E. Zhang and F. Liu, *On closed-form solutions to the generalized Sylvester-conjugate matrix equation*, Appl. Math. Comput., **218**(19) (2012), 9730-9741.
[11] I.M. Yaglom, *Complex numbers in geometry*, New York and London, Academic Press, 1968.
[12] I.M. Yaglom, *A simple non-Euclidean geometry and its physical basis*, New York, Springer Verlag, 1979.
[13] N. Gürses, M. Akbiyik and S. Yüce, *One-parameter homothetic motions and Euler-Savary formula in generalized complex number plane C_J*, Adv. Appl. Clifford Algebr., **26**(1) (2016), 115-136.
[14] F.S. Dündar, S. Ersoy and N.T.S. Pereira, *Bobillier formula for the elliptical harmonic motion*, An. St. Univ. Ovidius Constanta, **26**(1) (2018), 103-110.
[15] V. Brodsky and M. Shoham, *Dual numbers representation of rigid body dynamics*, Mech. Mach. Theory, **34**(5) (1999), 693-718.
[16] H.H. Cheng, *Programming with dual numbers and its applications in mechanisms design*, Eng. Comput., **10** (1994) 212-229.
[17] S. Ulrych, *Relativistic quantum physics with hyperbolic numbers*, Phys. Lett. B, **625**(3-4) (2005), 313-323.
[18] M. Kobayashi, *Hyperbolic hopfield neural networks*, IEEE Trans. Neural Netw. Learn. Syst., **24** (2013) 335-341.
[19] K. Özen and M. Tosun, *p-Trigonometric approach to elliptic biquaternions*, Adv. Appl. Clifford Algebr., **28**(62) (2018).
[20] J.H. Silverman, *The arithmetic of elliptic curve, Graduate Texts in Mathematics*, New York, 1988.
[21] S. Basu and D.J. Velleman, *On Gauss's first proof of the fundamental theorem of algebra*, Amer. Math. Monthly, **124**(8) (2017), 688-694.
[22] H.H. Kösal, *On the Commutative quaternion matrices*, Ph. D. Thesis, Sakarya University, 2016.
[23] A. Melman, *Modified Gershgorin discs for companion matrices*, Soc. Ind. Appl. Math., **54**(2) (2012), 355-373.
[24] Y.A. Alpin, M.T. Chien and L. Yeh, *The numerical radius and bounds for zeros of a polynomial*, Proc. Amer. Math. Soc., **131**(3) (2003), 725-730.
[25] H.E. Bell, *Gershgorin's theorem and the zeros of polynomials*, Amer. Math. Monthly, **72**(3) (1965), 292-295.
[26] A. Edelman and H. Murakami, *Polynomial roots from companion matrix eigenvalues*, Math. Comp., **64**(210) (1995), 763-776.
[27] H. Linden, *Bounds for the zeros of polynomials from eigenvalues and singular values of some companion matrices*, Linear Algebra Appl., **271**(1-3) (1998), 41-82.
[28] H.S Wilf, *Perron-Frobenius theory and the zeros of polynomials*, Proc. Amer. Math. Soc., **12** (1961), 247-250.

Journal of Mathematical Sciences and Modelling, 4 (3) (2021) 110-116
Research Article

Journal of Mathematical Sciences and Modelling

Journal Homepage: www.dergipark.gov.tr/jmsm
ISSN 2636-8692
DOI: http://dx.doi.org/10.33187/jmsm.1005520

Intersections of Multicurves on Small Genus Non–Orientable Surfaces

Saadet Öykü Yurttaş[1]

[1]*Dicle University Science Faculty Mathematics Department, 21280, Diyarbakır, Turkey*

Article Info

Keywords: *Geometric intersection, Generalized Dynnikov coordinates, Multicurves.*
2010 AMS: *57N16, 57M50.*
Received: *6 October 2021*
Accepted: *6 December 2021*
Available online: *29 December 2021*

Abstract

Let K_n $(n > 1)$ be an n–punctured non–orientable surface of genus 2 with 1 boundary component. We give formulae for calculating the geometric intersection number of an arbitrary multicurve with a relaxed multicurve on K_n given their generalized Dynnikov coordinates.

1. Introduction

Throughout the paper we work on a standard model of K_n $(n > 1)$ as depicted in Figure 1.1. That is, all the punctures and the crosscaps of K_n are aligned along the x-axis, and that each disk with an asterisk represents a crosscap, which is a graphical representation of a Möbius band (i.e. interior of such disks are removed and antipodal points on the remaining boundary are identified). We say that a simple closed curve in K_n is essential if it satisfies the following properties: it is not the core curve of a Möbius band and it doesn't bound an unpunctured disk, a once punctured disk or a Möbius band. A *multicurve* $\mathscr{L}$ is the homotopy class of a finite union of essential simple closed curves in K_n. We say that a multicurve is *relaxed* if each of its connected components intersects the x-axis at most twice (see for instance Figure 3.1). We denote by $\mathfrak{L}_n$ the set of multicurves in K_n. Let $\mathscr{L}_1, \mathscr{L}_2 \in \mathfrak{L}_n$. Then the geometric intersection number $\iota(\mathscr{L}_1, \mathscr{L}_2)$ is defined as

$$\min\{|L_1 \cap L_2| : L_1 \in \mathscr{L}_1, L_2 \in \mathscr{L}_2\}$$

where $|L_1 \cap L_2|$ denotes the number of intersections between L_1 and L_2.
The fact that the geometric intersection number is preserved under homeomorphisms yields a two step algorithm which works as follows. The first step of the algorithm is a relaxation algorithm finding a homeomorphism sending one of the multicurves to a relaxed one [1, 2] and the second provides formulae to calculate the geometric intersection number between an arbitrary multicurve and a relaxed one. This idea is realized in [1] for finitely many times punctured disks coordinatizing multicurves with Dynnikov coordinates and describing the action of the mapping class group (group of isotopy classes of homeomorphisms) using the update rules [3, 1]. In this paper we establish the second step of the aforementioned approach providing formula for each relaxed curve in K_n $(n > 1)$.
There are various combinatorial descriptions for multicurves on non–orientable surfaces [4, 5]. In this paper, we shall make use of the generalized Dynnikov coordinate system [5], which provides a one–to–one correspondence between $\mathfrak{L}_n$ and a certain subset of $\mathbb{Z}^{2n+2} \setminus \{0\}$, to generalize the approach in [2] for multicurves in K_n.
In Section 2 we present necessary terminology and background related with generalized Dynnikov coordinates of multicurves, and introduce some notions which will be important for developing the formulae stated in Section 3.

2. Generalized Dynnikov Coordinates of Multicurves

Consider the arcs α_i $(1 \leq i \leq 2n-2)$, β_i $(1 \leq i \leq n+1)$ and γ, and the core curves c_1, c_2 of crosscap 1 and crosscap 2 as shown in Figure 1.1. Given a multicurve $\mathscr{L} \in \mathfrak{L}_n$ we can always find a *taut* representative L of $\mathscr{L}$ that is a representative of $\mathscr{L}$ which intersects each of the arcs and curves minimally. We write $(\alpha; \beta; \gamma; c_1, c_2)$ for the set of intersection numbers of L with these arcs and curves.

Email addresses and ORCID numbers: **oyku1981@liv.ac.uk, 0000-0002-0262-1914 (S.Ö. Yurttaş)**

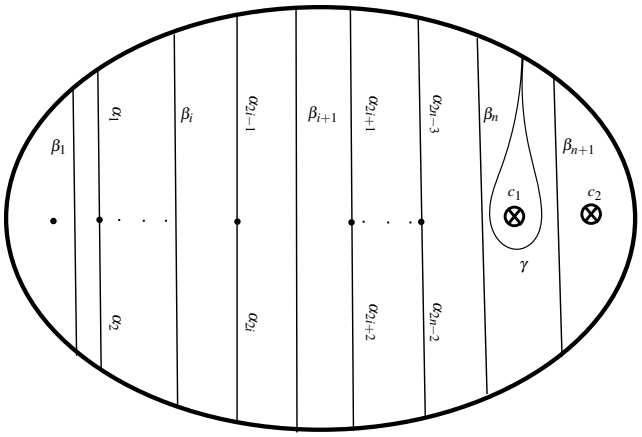

Figure 1.1: The arcs α_i, β_i, γ and curves c_1, c_2 on K_n

Let $1 \leq i \leq n-1$. Then S_i denotes the region which is a subset of K_n bounded by β_i and β_{i+1}, and contains puncture $i+1$. Note the special interpretation for S_0 which is bounded by the boundary and β_1. Let S_n denote the region bounded by β_n and β_{n+1}, and contains crosscap 1. Similarly, S_{n+1} contains crosscap 2 and bounded by the boundary and β_{n+1}. We write $S_{i,j} = \bigcup_{k=i}^{j} S_k$ for each i and j with $0 \leq i < j \leq n+1$. Then $S_{i,j}$ is the subset of K_n bounded by the arcs β_i and β_{j+1}. Note the special interpretation for $S_{0,j}$, $j \neq n+1$ (resp. $S_{i,n+1}$, $i \neq 0$) which is bounded by the boundary and β_{j+1} (resp. β_i).

Path components

Given a taut representative $L \in \mathscr{L} \in \mathfrak{L}_n$ we have the following possibilities of a connected component of $L \cap S_i$ and $L \cap S_{i,j}$:

Definition 2.1 (Above components)**.** *An above component of $L \cap S_i$ has one endpoint on β_i and the other on β_{i+1} passing under puncture $i+1$. Therefore, while it intersects the arc α_{2i-1} it does not intersect the arc α_{2i}. Similarly, an above component of $L \cap S_n$ has one endpoint on β_n and the other on β_{n+1} passing over crosscap 1. Therefore, it intersects the arc γ but not the core curve c_1. An above component of $L \cap S_{i,j}$ ($i \geq 1$, $j \leq n$) has one end point on β_i and the other on β_{j+1} and passing entirely over the x–axis.*

For example, in Figure 2.1 there are 2 above components of $L \cap S_i$ and 1 above component of $L \cap S_{i,j}$ for each $2 \leq j \leq n$.

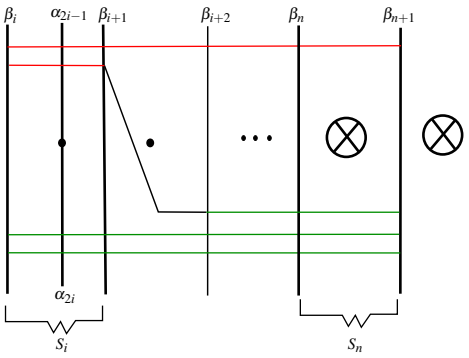

Figure 2.1: Above and below components denoted red and green respectively

Definition 2.2 (Below components)**.** *A below component of $L \cap S_i$ has one endpoint on β_i and the other on β_{i+1} passing under puncture $i+1$. Therefore, while it intersects the arc α_{2i} it does not intersect the arc α_{2i-1}. Similarly, a below component of $L \cap S_n$ has one endpoint on β_n and the other on β_{n+1} passing under crosscap 1. Therefore, it neither intersects the arc γ nor the core curve c_1. A below component of $L \cap S_{i,j}$ ($i \geq 1$, $j \leq n$) has one end point on β_i and the other on β_{j+1} and passing entirely below the x–axis.*

For example, in Figure 2.1 there are 2 below components of $L \cap S_i$ and $L \cap S_{i,j}$ for each $2 \leq j \leq n$.

Definition 2.3 (Left loop components)**.** *A left loop component of $L \cap S_i$ intersects each α_k ($k = 2i, 2i-1$) exactly once and has each of its endpoints on β_{i+1}. Similarly, a left loop component of $L \cap S_n$ intersects γ exactly twice having each of its end points on β_{n+1}. If it intersects the core curve c_1, we call it a left core loop component, and if it doesn't we call it a left non-core loop component. A left loop component of $L \cap S_{i,j}$, $j \leq n-1$ intersects the x–axis between β_i and the puncture $i+1$ having each of its end points on β_{j+1}. A left loop component of $L \cap S_{i,n}$ intersects the x–axis between β_i and the puncture $i+1$ having each of its end points on β_{n+1}. There are no left loop components of $L \cap S_{i,n+1}$ since there are no above or below components of $L \cap S_{n+1}$.*

Definition 2.4 (Right loop components)**.** *A right loop component of $L\cap S_i$ intersects each α_k ($k=2i,2i-1$) exactly once and has each of its endpoints on β_i. Similarly, a right loop component of $L\cap S_n$ intersects γ exactly twice having each of its end points on β_n. If it intersects the core curve c_1, we call it a right core loop component, and if it doesn't we call it a right non-core loop component. A right loop component of $L\cap S_{i,j}$, $j\leq n-1$ intersects the x–axis between β_{j+1} and the puncture $j+1$ having each of its end points on β_i. A right loop component of $L\cap S_{i,n}$, $i\geq 1$ (respectively $L\cap S_{i,n+1}$) intersects the x–axis only between crosscap 1 (respectively crosscap 2) and β_{n+1} (respectively the boundary) having each of its end points on β_i. There are no right loop components of $L\cap S_{0,j}$ since there are no above or below components of $L\cap S_0$.*

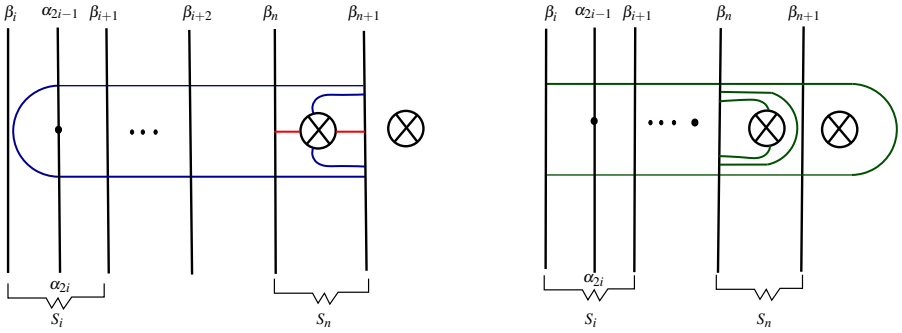

Figure 2.2: Examples for left and right loop components

Definition 2.5 (Straight core components)**.** *A straight core component of $L\cap S_n$ intersects c_1 exactly once having one of its endpoints on β_n and the other on β_{n+1}. There are no straight core components of $L\cap S_{n+1}$.*

Consider for example the left hand side of Figure 2.2. We have 1 left loop component of $L\cap S_i$, 1 core loop component and 1 straight core component (depicted red) of $L\cap S_n$ and 1 left loop component of $L\cap S_{i,j}$ for each $2\leq j\leq n$. Similarly, consider the right hand side of Figure 2.2. We have 1 right core and 1 right non–core loop component $L\cap S_n$ and 1 right loop component of $L\cap S_{i,n+1}$.
See Lemma 2.3 and Lemma 2.4 in [5] for the proofs of the following lemmas.

Lemma 2.6. *Let $1\leq i\leq n$. There are $\left|b_i=\frac{\beta_i-\beta_{i+1}}{2}\right|$ loop components of $L\cap S_i$. If $b_i>0$ the loop components are right and if $b_i<0$ they are left. The number of loop components of $L\cap S_0$ is given by $\frac{\beta_1}{2}$, and the number of right loop components of $L\cap S_{n+1}$ is given by $\frac{\beta_{n+1}}{2}$. We denote by λ_{c_i} and λ_i the number of core loop and non–core loop components of $L\cap S_i$ ($i=n,n+1$), and by ψ the number of straight core components of $L\cap S_n$.*

$$\begin{aligned}
&\lambda_1=\max(|b_n|-c_1,0) \quad \textit{and} \quad \lambda_{c_1}=\min(|b_n|,c_1)\\
&\lambda_2=\frac{\beta_{n+1}}{2}-c_2 \qquad\qquad \textit{and} \quad \lambda_{c_2}=c_2\\
&\psi=\max(c_1-|b_n|,0).
\end{aligned}$$

Since above and below components of $L\cap S_i$ intersect α_{2i-1} and α_{2i} respectively; and above and below components of $L\cap S_n$ pass above and below crosscap 1 respectively, and that below and above components of $L\cap S_{i,j}$ form the lowest and highest components of each $L\cap S_i$ respectively we immediately get Lemma 2.7.

Lemma 2.7. *Denote by B_k and A_k the number of below and above components of $L\cap S_k$ ($1\leq k\leq n$). Let $B_{i,j}$ and $A_{i,j}$ denote the number of below and above components of $L\cap S_{i,j}$ respectively. Then, we have*

$$\begin{aligned}
&A_i=\alpha_{2i-1}-|b_i| \quad \textit{and} \quad B_i=\alpha_{2i}-|b_i|, \quad \textit{for} \quad 1\leq i\leq n-1\\
&A_n=\frac{\gamma}{2}-|b_n|-\psi \quad \textit{and} \quad B_n=\max(\beta_{n+i},\beta_{n+i+1})-|b_n|-\frac{\gamma}{2}\\
&A_{i,j}=\min_{i\leq k\leq j}A_k \quad \textit{and} \quad B_{i,j}=\min_{i\leq k\leq j}B_k
\end{aligned}$$

Notation 1. *Let λ_k ($k=1,2$) be as given in Lemma 2.6. We write*

$$\lambda_1^+=\begin{cases}\lambda_1 & \textit{if } b_n>0\\ 0 & \textit{if } b_n<0\end{cases} \quad \textit{and} \quad \lambda_i^-=\begin{cases}\lambda_i & \textit{if } b_n<0\\ 0 & \textit{if } b_n>0\end{cases}$$

We set $\lambda_2^+=\lambda_2$ since there are only right loop components of $L\cap S_{n+1}$.

2.1. The generalized Dynnikov coordinates

The function $\rho\colon \mathfrak{L}_n \to \mathbb{Z}^{2n+2}\setminus\{0\}$ defined by

$$\rho(\mathscr{L}) = (a;b;t;c_1,c_2) := (a_1,\ldots,a_{n-1};b_1,\ldots,b_n;t;c_1,c_2)$$

where

$$a_i = \frac{\alpha_{2i}-\alpha_{2i-1}}{2}; 1\le i\le n-1, \qquad b_i = \frac{\beta_i-\beta_{i+1}}{2}; 1\le i\le n, \qquad t = A_n - B_n, \tag{2.1}$$

where A_n and B_n are as given in Lemma 2.7 is called the generalized Dynnikov coordinate function.

Notation 2. *Let $\mathscr{S} = \mathbb{Z}^{2n+2}\setminus\{0\}$ and $\mathscr{S}_1 = \{(a;b;t;c_1,c_2) :\in \mathscr{S} : |t|+\psi \quad \text{is even}\}$ where ψ is as given in Lemma 2.6.*

Next, we give Theorem 2.8 [5] which presents formulae to compute the intersection numbers $(\alpha;\beta;\gamma;c_1,c_2)$ from the generalized Dynnikov coordinates $(a;b;t;c_1,c_2)$; and hence reconstructs the corresponding multicurve as depicted in Figure 2.3.

Theorem 2.8. *Let $(a;b;t;c_1,c_2)\in\mathscr{S}_1$, and*

$$X = 2\max_{1\le r\le n-1}\left\{|a_r| + \max(b_r,0) + \sum_{j=1}^{r-1} b_j\right\}$$
$$Y = \left\{|t| + 2\max(b_n,0) + \psi + 2\sum_{j=1}^{n-1} b_j\right\}$$
$$\beta_i^* = \max(X,Y) - 2\sum_{j=1}^{i-1} b_j \quad \text{and} \quad R = \max(0, 2c_2 - \beta_{n+1}^*)$$

Then $(a;b;t;c_1;c_2)$ is the generalized Dynnikov coordinate of exactly one element $\mathscr{L}\in\mathfrak{L}_n$ with

$$\beta_i = \beta_i^* + 2R$$
$$\alpha_i = \begin{cases} (-1)^i a_{\lceil i/2\rceil} + \frac{\beta_{\lceil i/2\rceil}}{2} & \text{if } b_{\lceil i/2\rceil}\ge 0, \\ (-1)^i a_{\lceil i/2\rceil} + \frac{\beta_{1+\lceil i/2\rceil}}{2} & \text{if } b_{\lceil i/2\rceil}\le 0, \end{cases}$$
$$\gamma = 2(A_n + |b_n| + \psi).$$

Example 2.9. *Let $\mathscr{L}\in\mathfrak{L}_2$ be a multicurve with generalized Dynnikov coordinates $\rho(\mathscr{L}) = (2;1,0;-2;2,0)$. Theorem 2.8 gives that $\mathscr{L}$ has intersection numbers $\alpha_1=1$, $\alpha_2=5$, $\beta_1=6$, $\beta_2=4$, $\beta_3=4$, $\gamma=4$. From Lemma 2.6 and Lemma 2.7 we get that $b_1=1$ and $b_2=0$ that is there is one right loop component of $L\cap S_1$ and no loop components of $L\cap S_2$; $A_1=0, B_1=4$ that is there are four below components and no above components of $L\cap S_1$; and $A_2=0, B_2=2$ that is there are 2 below components and no above components of $L\cap S_2$. Also, $\lambda_2=2, \lambda_{c_2}=0$ and hence there are no core loop components of $L\cap S_2$ and two core loop components of $L\cap S_2$. Pasting the pieces of these connected components in each region together uniquely determine the curve as depicted in Figure 2.3.*

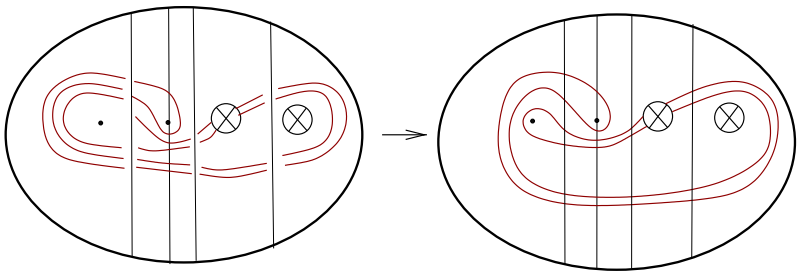

Figure 2.3: Gluing components of $L\cap S_i$ together determines $\mathscr{L}$ uniquely up to homotopy

3. Geometric intersection of multicurves with relaxed curves

Definition 3.1 (Relaxed curves)**.** *A relaxed curve in K_n is the homotopy class of an essential simple closed curve in K_n which intersects the x–axis at most twice, and is represented by one of the following curves:*

- *$\mathscr{C}_{i,j}$ is contained in the region $S_{i,j}$. It has $\rho(\mathscr{C}_{i,j}) = (0;b;0;0)\in\mathscr{S}_1$ such that if $0<i<j<n+1$, $b_i=-1$ and $b_j=1$. If $i=0$ each $b_k=0$ except for $b_j=1$, and if $j=n+1$, each $b_k=0$ except for $b_i=-1$.*
- *$\mathscr{D}$ is contained in the region $S_{n,n+1}$. It has $\rho(\mathscr{D}) = (0;b;0;c)\in\mathscr{S}_1$ such that $b_j=0$ $(1\le j\le n-1)$ and $b_n=-1$, $b_{n+1}=1$ and $c_1=c_2=1$.*

Notation 3. *For convenience we shall denote by $\mathscr{C}$ the homotopy class of the relaxed curve bounding both crosscap 1 and crosscap 2.*

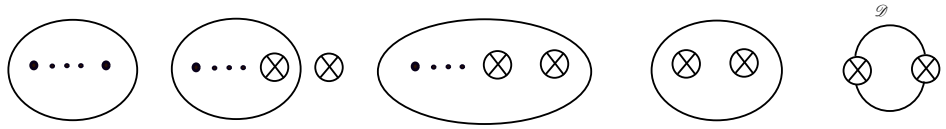

Figure 3.1: Some relaxed curves $\mathscr{C}_{i,j}$ and $\mathscr{D}$ on K_n

Note that different values for indices i and j give different topological types of curves. Some examples for relaxed curves in K_n are illustrated in Figure 3.1. A multicurve $\mathscr{L} \in \mathfrak{L}_n$ is relaxed if each of its components is relaxed.

Notation 4. *Let λ_j^+ $(j = n, n+1)$ and λ_j^- $(j = n)$ be as given in Notation 1. For the sake of brevity we shall write $b_j = \lambda_j$ for $1 \leq j \leq n$ (this is always possible since there are no core loops about puncture j).*

Lemma 3.2. *Let $1 \leq i < j \leq n$. There are R right and L left loop components of $L \cap S_{i,j}$ respectively given by*

$$R = \min(A_{i,j-1} - A_{i,j},\ B_{i,j-1} - B_{i,j},\ \lambda_j^+), \quad \textit{and}$$
$$L = \min(A_{i+1,j} - A_{i,j},\ B_{i+1,j} - B_{i,j},\ \lambda_i^-).$$

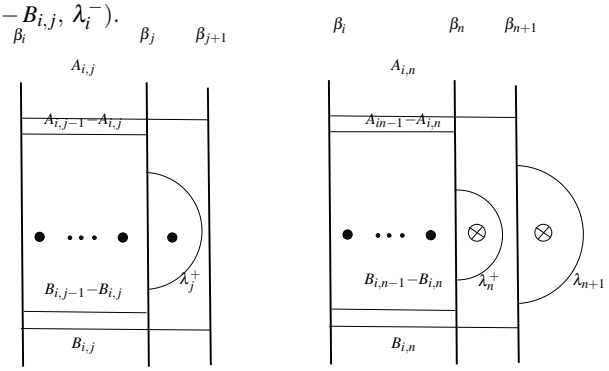

Figure 3.2: Calculation of right loop components of $L \cap S_{i,j}$

Proof. Consider the above components of $S_{i,j-1}$ which are not contained in above components of $L \cap S_{i,j}$. Number of such components is given by $A_{i,j-1} - A_{i,j}$. Similarly, number of below components of $S_{i,j-1}$ which are not contained in below components of $L \cap S_{i,j}$ is given by $B_{i,j-1} - B_{i,j}$. Since there are λ_j^+ non–core loop components of S_j $(j = n, n+1)$ it is immediate from Figure 3.2 that R is the minimum of these three numbers. Number of left loop components of $L \cap S_{i,j}$ is calculated similarly.

□

Theorem 3.3 (Intersections with $\mathscr{C}_{i,j}$)**.** *Let $\mathscr{L} \in \mathscr{L}_n$ be a multicurve with $\rho(\mathscr{L}) = (a; b; t; c_1, c_2) \in \mathscr{S}_1$. Let $0 \leq i < j \leq n$ with $(i, j) \neq (0, n+1)$. Then the geometric intersection number $\iota(\mathscr{L}, \mathscr{C}_{i,j})$ is given by*

$$\iota(\mathscr{L}, \mathscr{C}_{i,j}) = \beta_i + \beta_{j+1} - 2(R + L + A_{i,j} + B_{i,j}).$$

Proof. Let $\gamma_{i,j}$ be a taut representative of the relaxed curve $\mathscr{C}_{i,j}$, and let L be a taut representative of $\mathscr{L}$ with respect to each arc $\alpha_i, \beta_i, \gamma$, each curve c_i, and to $\gamma_{i,j}$. With the set up in Section 2 the proof is identical to that of Lemma 7 in [1] which is based on computing explicitly the number of connected components of $L \cap S_{i,j}$ which are disjoint from $\gamma_{i,j}$. We first note that the number of connected components of $L \cap S_{i,j}$ that are not simple closed curves is given by $\frac{\beta_i + \beta_{j+1}}{2}$. Each such component either has zero intersection with $\gamma_{i,j}$ or intersects it twice. Those which are disjoint from $\mathscr{C}_{i,j}$ are above, below, left and right loop components of $L \cap S_{i,j}$ (Figure 3.3) number of which are given by $A_{i,j}$, $B_{i,j}$, L and R respectively as given above. Therefore, we get

$$\iota(\mathscr{L}, \mathscr{C}_{i,j}) = \beta_i + \beta_{j+1} - 2(R + L + A_{i,j} + B_{i,j})$$

as required.

□

Theorem 3.4. *Let $\mathscr{L} \in \mathscr{L}_n$ be a multicurve with $\rho(\mathscr{L}) = (a; b; t; c_1, c_2) \in \mathscr{S}_1$. Let $\iota(\mathscr{L}, \mathscr{C})$ and $\iota(\mathscr{L}, \mathscr{D})$ denote the geometric intersection numbers between $\mathscr{L}$ and the relaxed curves $\mathscr{C}$ and $\mathscr{D}$ respectively. Then,*

$$\iota(\mathscr{L}, \mathscr{D}) = \begin{cases} \iota(\mathscr{L}, \mathscr{C}) & ;\ c_1 = c_2 = 0, \\ |c_1 - c_2| & ;\ \textit{otherwise} \end{cases}$$

Proof. There are two cases: Either $c_1 = c_2 = 0$ or $c_i \neq 0$ for some $k \in \{1, 2\}$. The former case is immediate from Figure 3.4(a). For the latter case assume without loss of generality that $c_1 \geq c_2$. Then any curve intersecting c_1 must intersect c_2 or $\mathscr{D}$ as illustrated in Figure 3.4(b) and Figure 3.4(c). That is, $c_1 = \mathscr{D} + c_2$ as required. □

Example 3.5. *Let $\mathscr{L} \in \mathfrak{L}_2$ be a multicurve with $\rho(\mathscr{L}) = (-1; 1, 0; 1; 1, 1)$ (Figure 3.5). By Theorem 2.8, $\mathscr{L}$ has intersection numbers $(\alpha_1, \alpha_2; \beta_1, \beta_2, \beta_3; \gamma_1; c_1, c_2) = (3, 1; 4, 2, 2; 4; 1, 1)$. Since $c_1 = c_2 = 0$, we get from Theorem 3.4 that $\iota(\mathscr{L}, \mathscr{D}) = |c_1 - c_2| = 0$.*

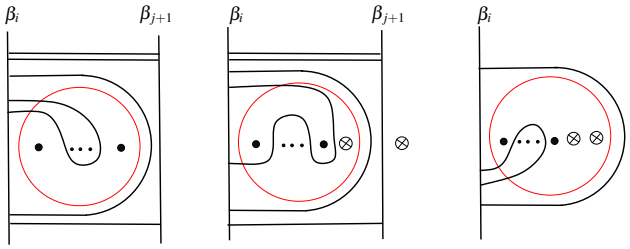

Figure 3.3: Connected components of $L \cap S_{i,j}$ that are disjoint from $\mathscr{C}_{i,j}$

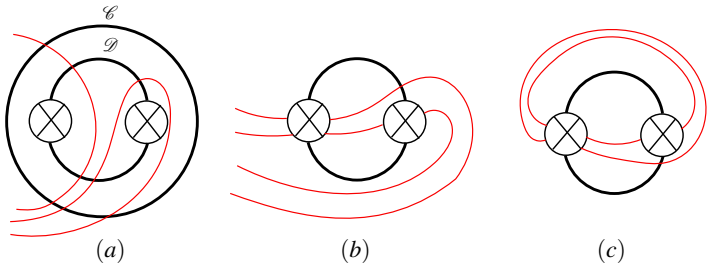

Figure 3.4: Proof for $\mathscr{D}$

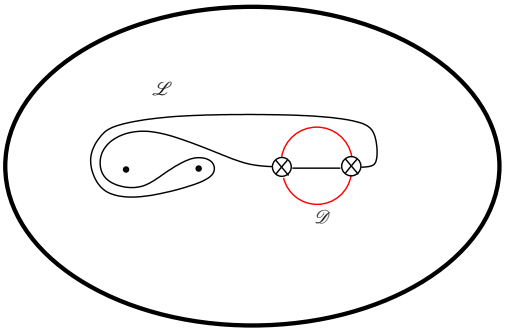

Figure 3.5: $\iota(\mathscr{L}, \mathscr{L}_2) = 0$

4. Conclusion

The results stated in Theorem 3.3 and Theorem 3.4 are obtained only for genus 2 non–orientable surfaces in this paper. We note that the formulae for relaxed curves which have zero intersection with the crosscaps can be generalized to a higher genus non–orientable surface N immediately using the similar techniques given in Theorem 3.3. Similarly, the formula for $\mathscr{D}$ can be used for the two sided curves $\mathscr{F}_{i,i+1}$ on N which intersects crosscap i and crosscap $i+1$ exactly once, and has zero intersection with the diameter of the surface. However, for relaxed curves $\mathscr{F}_{i,j}$ on N which intersects crosscaps i through j $(j > i+1)$ the method given in Theorem 3.4 fails. The main reason the method doesn't work is that if the arcs intersecting $\mathscr{F}_{i,j}$ are complicated, then it is far from straightforward to describe components which are disjoint from $\mathscr{F}_{i,j}$ or to determine a relation between the number of intersections on $\mathscr{F}_{i,j}$, the core curves and the other relaxed curves $\mathscr{C}_{i,j}$.

Question 1. *Generalize the geometric intersection formulae between arbitrary curves and relaxed curves for higher genus non–orientable surfaces. In particular, what is the formula for $\mathscr{L} \in \mathfrak{L}_{g,n}$ and the relaxed curves $\mathscr{F}_{i,j}$ $(j > i+1)$ in terms of their generalized Dynnikov coordinates on higher genus surfaces?*

Acknowledgements

The author would like to express her sincere thanks to the editor and the anonymous reviewers for their helpful comments and suggestions. The author would also like to thank Ferihe Atalan for her valuable comments on an earlier version of this paper.

Funding

This work was supported by TÜBİTAK (project number 3001-117F282).

Availability of data and materials

Not applicable.

Competing interests

The authors declare that they have no competing interests.

References

[1] T. Hall, S. Ö. Yurttaş, *Intersections of multicurves from Dynnikov coordinates*, Bull. Aust. Math. Soc, **98**, (2018), 149-158.
[2] S. Ö. Yurttaş, *Geometric intersection of curves on punctured disks*, J. Math. Soc. Japan, **65**(4) (2013), 1153-1168.
[3] I. Dynnikov, *On a Yang-Baxter mapping and the Dehornoy ordering*, Uspekhi Mat. Nauk, **57**(345) (2002), 151-152.
[4] A. Papadopoulos, R.C. Penner, *Hyperbolic metrics, measured foliations and pants decompositions for non-orientable surfaces*, Asian J. Math, **20** (2016), 157-182.
[5] M. Pamuk, S. Ö. Yurttaş, *Integral laminations on non–orientable surfaces*, Turkish J. Math, **42** (2018), 69-82.

Journal of Mathematical Sciences and Modelling, 4 (3) (2021) 117-125
Research Article

Journal of Mathematical Sciences and Modelling

Journal Homepage: www.dergipark.gov.tr/jmsm
ISSN 2636-8692
DOI: http://dx.doi.org/10.33187/jmsm.1012850

Vortex Solitons on Partially $\mathscr{P}\mathscr{T}$-symmetric Azimuthal Lattices in a Medium with Quadratic Nonlinear Response

Mahmut Bağcı[1]

[1]*Department of Software Development, School of Applied Sciences, Yeditepe University, Istanbul, Turkey*

Article Info

Keywords: *Partially Parity-time-symmetric, Quadratic nonlinear media, Vortex solitons*
2010 AMS: *47J35, 35Q55, 81Q05*
Received: *21 October 2021*
Accepted: *16 November 2021*
Available online: *29 December 2021*

Abstract

Vortex solitons in parity-time ($\mathscr{P}\mathscr{T}$) symmetric and partially $\mathscr{P}\mathscr{T}$ (p$\mathscr{P}\mathscr{T}$) symmetric azimuthal lattices are demonstrated for a media with quadratic nonlinear response. Stability properties of the vortices are investigated comprehensively by linear spectra and nonlinear evolution of the governing equations, and it is shown that, although the existence domain of the $\mathscr{P}\mathscr{T}$-symmetric and p$\mathscr{P}\mathscr{T}$-symmetric lattices are identical, the stability region of $\mathscr{P}\mathscr{T}$-symmetric lattice is narrower than that of the p$\mathscr{P}\mathscr{T}$-symmetric lattice. It is also observed that deeper real part in the azimuthal potentials supports stability of vortex solitons, whereas deeper imaginary part and strong quadratic electro-optic effects impoverish stability properties of the vortices. Moreover, it is shown that there are different stability properties of vortices in p$\mathscr{P}\mathscr{T}$-symmetric azimuthal potentials for different vorticity values, while there is no such difference for vortices in $\mathscr{P}\mathscr{T}$-symmetric potentials.

1. Introduction

Solitons are localized waves that arise from a balance between nonlinear and dispersive effects in the medium, and they maintain their shape and velocity during propagation. In the same manner, vortex solitons preserve their angular momentum during propagation. In recent years, there has been considerable attention to soliton dynamics in optically induced lattices (potentials). These external lattices can be perfectly periodic [1, 2], quasi-periodic [3, 4] or irregular structures that possess point or line defects [5].

It is known that if the optical systems include energy gain and loss, the potential of the medium would be complex [6], and such potentials are called parity-time ($\mathscr{P}\mathscr{T}$) symmetric. A complex potential $V(x,y)$ is $\mathscr{P}\mathscr{T}$-symmetric, if it satisfies the condition $V^*(x,y) = V(-x,-y)$ [6, 7]. In 1998, Bender and Boettcher showed that non-Hermitian Hamiltonians can produce entirely real spectra when they are ($\mathscr{P}\mathscr{T}$) symmetric [8], and this fact reveals stable propagation of the solitons in optical systems with $\mathscr{P}\mathscr{T}$-symmetric lattices under suitable conditions [9]. $\mathscr{P}\mathscr{T}$-symmetric lattices were observed experimentally in [10]-[12] and theoretically in [7], and pulse dynamics in $\mathscr{P}\mathscr{T}$-symmetric optical systems are investigated in many studies [13]-[18].

Recently, it has been demonstrated that the spectrum of a complex potential may remain real even if the potential is invariant under complex conjugation and reflection in a single spatial direction (i.e., $V^*(x,y) = V(-x,y)$ or $V^*(x,y) = V(x,-y)$), which means the complex potential is partially $\mathscr{P}\mathscr{T}$-symmetric (p$\mathscr{P}\mathscr{T}$-symmetric) [19, 20]. Soliton dynamics in such p$\mathscr{P}\mathscr{T}$-symmetric lattices have been investigated [20], and symmetry breaking of solitons in p$\mathscr{P}\mathscr{T}$-symmetric potentials has been demonstrated by Yang [13, 19]. Symmetry breaking is observed above a critical power, and this power threshold is a bifurcation point after which non-$\mathscr{P}\mathscr{T}$-symmetric (asymmetric) solitons can exist. More recently, vortex solitons in p$\mathscr{P}\mathscr{T}$-symmetric azimuthal potentials have been introduced in [21], and it is shown that although the considered azimuthal potentials are p$\mathscr{P}\mathscr{T}$-symmetric, symmetry breaking of the lattice is not observed. Accordingly, it is shown that stable vortex solitons can be obtained in p$\mathscr{P}\mathscr{T}$-symmetric potentials, where the symmetry is already broken in the $\mathscr{P}\mathscr{T}$-symmetric counterpart of the potential. The p$\mathscr{P}\mathscr{T}$-symmetric azimuthal potentials are constructed from $\mathscr{P}\mathscr{T}$-symmetric cells placed on a ring where azimuthal directions (vorticity) become nonequivalent, and the nonequivalence of the azimuthal directions causes remarkable effects on the properties of vortex solitons. Different from vortices in conservative systems, nonequivalent vorticity of the p$\mathscr{P}\mathscr{T}$-symmetric potentials causes the disparity of the gain loss distribution along the azimuthal direction. In [21], different internal current distributions have been demonstrated for vortices in such p$\mathscr{P}\mathscr{T}$-symmetric azimuthal potentials.

Email addresses and ORCID numbers: bagcimahmut@gmail.com, 0000-0001-6931-6837 (M. Bağcı)

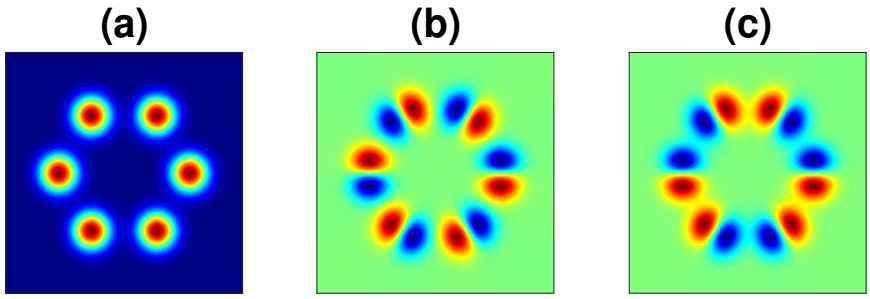

Figure 2.1: Top view of the azimuthal lattices within $(x,y) \in [-4,4]$. (a) Real part V_{re}; (b) Imaginary part (V_{im}) of p$\mathscr{PT}$-symmetric potential when $\sigma = 1$; (c) Imaginary part (V_{im}) of $\mathscr{PT}$-symmetric potential when $\sigma = -1$. The real parts of potentials are identical.

In the abovementioned studies, soliton dynamics of the $\mathscr{PT}$-symmetric and p$\mathscr{PT}$- symmetric lattices have been investigated in cubic nonlinear (Kerr) media that is governed by nonlinear Schrödinger (NLS) type equations. However, it is known that many nonlinear optical systems include materials, such as potassium niobate ($KNbO_3$) [22] or lithium niobate ($LiNbO_3$) [23], that have both cubic and quadratic nonlinear responses [24, 25]. One of the models to describe the nonlinear evolution of the optical waves in quadratically polarized media is the NLS equation with coupling to a mean term (denoted as NLSM systems). The NLSM equations were introduced to characterize water waves by Benney and Roskes in 1969 [26] and extended to three-dimensional wave packets by Davey and Stewartson in 1974 [27], then Ablowitz *et al.* [24, 28, 29] derived an equivalent form of the NLSM model to characterize the pulse dynamics in non-resonant quadratic materials. Recently, the existence of ground-state solution for the NLSM system was demonstrated and collapse dynamics were investigated [30] and it was shown that wave collapse in the NLSM system can be arrested by self-rectification [22]. Latterly, collapse of the NLSM system has been arrested by real periodic [31], quasiperiodic [32] and p$\mathscr{PT}$-symmetric [33] external lattices. The general NLSM system is defined as [22, 28, 29]

$$iu_z + \Delta u + |u|^2 u - \rho u\phi = 0, \qquad \phi_{xx} + \nu\phi_{yy} = \left(|u|^2\right)_{xx}$$

where $u(x,y)$ is the normalized amplitude of the envelope of the normalized static electric field propagating in the z direction. $\Delta u \equiv u_{xx} + u_{yy}$ corresponds to diffraction, and the cubic term in u originates from the nonlinear (Kerr) change of the refractive index. ρ denotes the combined optical rectification and electro-optic effects modeled by the $\phi(x,y)$ field, and ν shows the anisotropy of the material.

These equations come from the interplay between the fundamental and dc fields while the second-harmonic-generation (SHG) is not phase matched. In such circumstances, an additional self-phase modulation contribution is produced by the SHG due to cascaded nonlinearity. Consequently, the NLSM system is a nonlocal nonlinear coupling between the first field and a static field that is emerged from the zeroth harmonic (mean term) [24, 28, 29].

In this study, the numerical existence of vortex solitons in $\mathscr{PT}$-symmetric and p$\mathscr{PT}$-symmetric azimuthal lattices are demonstrated for a medium with quadratic nonlinear response, and stability properties of the obtained vortex solitons are investigated comprehensively by linear spectrum and nonlinear evolution of the governing equations. The model equations are given as the NLSM system with an additional external potential. The paper is outlined as follows: In Sec. 2, the model equations and the azimuthal potentials are presented, and vortex soliton solutions of the model are obtained by numerical methods. In Sec. 3, stability of the vortex solitons are examined by the nonlinear evolution and linear stability spectra of the model, and impact of the vorticity on vortex stability is investigated. Results of the study is summarized in Sec. 4.

2. The Model

Pulse dynamics in a medium with quadratic nonlinear response and an additional external potential is governed by the following (2+1) dimensional model

$$iu_z + \Delta u + |u|^2 u - \rho u\phi + [p_{re}V_{re}(x,y) - ip_{im}V_{im}(x,y)]u = 0, \qquad \phi_{xx} + \nu\phi_{yy} = \left(|u|^2\right)_{xx} \tag{2.1}$$

where p_{re} and p_{im} are the depths of real and imaginary parts of the complex potential $V(x,y)$, respectively. The potential $V(x,y)$ is defined as N Gaussian waveguides that are placed on a ring of radius r_0 [21]:

$$V_{re} = \sum_{k=1}^{N} e^{-[(x-r_0\cos\theta_k)^2+(y-r_0\sin\theta_k)^2]/\alpha^2}$$
$$V_{im} = \sum_{k=1}^{N} \sigma^{k-1}(y\cos\theta_k - x\sin\theta_k)e^{-[(x-r_0\cos\theta_k)^2+(y-r_0\sin\theta_k)^2]/\alpha^2}$$

where $\sigma = \pm 1$, $\theta_k = 2\pi(k-1)/N$ and α is waveguide width. For $\sigma = -1$ the potential is $\mathscr{PT}$-symmetric, i.e., $V(x,y) = V(-x,y) = V^*(x,-y) = V^*(-x,-y)$, and for $\sigma = 1$, it is p$\mathscr{PT}$-symmetric, i.e., $V(x,y) = V^*(-x,y) = V^*(x,-y) \neq V^*(-x,-y)$. We consider $\mathscr{PT}$ and p$\mathscr{PT}$-symmetric azimuthal potentials with $N = 6$, the radius $r_0 = N/2$ and the waveguide width $\alpha = 0.5$. Real and imaginary parts of $\mathscr{PT}$ ($\sigma = -1$) and p$\mathscr{PT}$-symmetric ($\sigma = 1$) azimuthal potentials are displayed in Figure 2.1. The phase transition point was determined as $p_{im} = 7.2$ for $\mathscr{PT}$-symmetric case of the lattice when $p_{re} = 5$ [21]. Above this threshold value, spectrum of the lattice include eigenvalues with non-zero imaginary parts. Phase transition is not observed for the p$\mathscr{PT}$-symmetric azimuthal potential (when $\sigma = 1$).

2.1. Numerical solution for the vortex solitons

The steady state solution (vortex solitons) of the considered model (2.1) is obtained via squared operator method (SOM) that has been developed by Yang [34]. It has been shown that steady state solutions of a wide range of nonlinear wave equations can be computed efficiently by the SOM algorithm. The algorithm is outlined as follows:
Inserting the ansatz $u = U(x,y)\exp(i\mu z)$ into the system (2.1), the operator $\mathbf{L}_0$ is obtained,

$$\mathbf{L}_0\mathbf{u} = -\mu U + \Delta U + |U|^2 U - \rho\phi U + VU, \qquad \phi_{xx} + \nu\phi_{yy} = \left(|U|^2\right)_{xx}$$

where μ is the eigenvalue (propagation constant). Splitting the operator $\mathbf{L}_0$ into its real and imaginary parts and applying Fourier transformation, we get the sub-operators $T1$ and $T2$ as follows:

$$T1 = \mathrm{Re}\left(\mathscr{F}^{-1}\left(\frac{\mathscr{F}(\mathbf{L}_0\mathbf{u})}{K^2+c}\right)\right), \qquad T2 = \mathrm{Im}\left(\mathscr{F}^{-1}\left(\frac{\mathscr{F}(\mathbf{L}_0\mathbf{u})}{K^2+c}\right)\right).$$

where $\mathscr{F}$ denotes Fourier transformation, $k = (k_x, k_y)$ are Fourier variables, $K^2 = k_x^2 + k_y^2$ and c is a real positive number that is chosen heuristically for parametrizing the algorithm. Separating the amplitue U into its real and imaginary parts $U = U_{re}(x,y) + iU_{im}(x,y)$ and substituting into the operator $\mathbf{L}_0\mathbf{u}$ (2.2), we get sub-operators L_{Re} and L_{Im} as follows:

$$L_{\mathrm{Re}} = -\mu U_{re} + \Delta U_{re} + (U_{re}^3 + U_{re}U_{im}^2) - \rho\phi U_{re} + p_{re}V_{re}U_{re} + p_{im}V_{im}U_{im}$$

$$L_{\mathrm{Im}} = -\mu U_{im} + \Delta U_{im} + (U_{im}^3 + U_{re}^2 U_{im}) - \rho\phi U_{im} + p_{re}V_{re}U_{im} - p_{im}V_{im}U_{re}.$$

Taking partial derivatives of L_{Re} and L_{Im} with respect to both U_{re} and U_{im} gives elements of the operator $\mathbf{L}_1$,

$$R_{11} = \frac{\partial L_{\mathrm{Re}}}{\partial U_{re}}(T1), \quad R_{12} = \frac{\partial L_{\mathrm{Re}}}{\partial U_{im}}(T2),$$

$$R_{21} = \frac{\partial L_{\mathrm{Im}}}{\partial U_{re}}(T1), \quad R_{22} = \frac{\partial L_{\mathrm{Im}}}{\partial U_{im}}(T2).$$

and the operator $\mathbf{L}_1$ is defined as

$$\mathbf{L}_1\mathbf{u} = R_{11} + R_{12} + i(R_{21} + R_{22}).$$

After $\mathbf{L}_0$ and $\mathbf{L}_1$ are obtained, the algorithm is iterated as follows,

$$U_{n+1} = U_n - \left(\mathscr{F}^{-1}\left(\frac{\mathscr{F}(\mathbf{L}_1\mathbf{u})}{K^2+c}\right)\right)\Delta t,$$

$$\mu_{n+1} = \mu_n + \|u\cdot T1 + v\cdot T2\|\Delta t,$$

$$\phi_{n+1} = \mathscr{F}^{-1}\left(\frac{k_x^2\mathscr{F}\left(|U_n|^2\right)}{k_x^2+\nu k_y^2}\right).$$

This numerical scheme is implemented until the error

$$E = \sqrt{\|U_{n+1} - U_n\|^2} + |\mu_{n+1} - \mu_n| < 10^{-8},$$

and this algortihm is convergent while the time step Δt is below a certain threshold [34].
To obtain vortex solitons of the model (2.1), the initial condition of the SOM algorithm is chosen as

$$u(x,y,z) = U(\mathbf{r})exp[im\theta(\mathbf{r}) + i\mu z] \tag{2.2}$$

where $\mathbf{r} = (x,y)$, U is field module, θ is the phase, m is vorticity and μ is the propagation constant. The considered azimuthal potentials ($N = 6$) support six-hump vortex solitons for the following parameter set:

$$(\rho, \nu, p_{re}, p_{im}, \mu, m) = (0.5, 1.5, 6, 1, 0.5, 1). \tag{2.3}$$

It is noted that $\rho = 0.5$ and $\nu = 1.5$ are particularly selected parameter values to characterize quadratic electro-optic effects in potassium niobate ($KNbO_3$) [22].
In Figure 2.2, the vortex profile, the top view and the phase structure are shown for the azimuthal potentials when $\sigma = 1$ (p$\mathscr{P}\mathscr{T}$-symmetric) in the first row (a) and when $\sigma = -1$ ($\mathscr{P}\mathscr{T}$-symmetric) in the second row (b). It can be seen that there are six-hump vortex structures that are located at local maxima of the considered azimuthal potentials.

3. Power and Stability Analysis

The vortex solutions of the model (2.1) is computed by the SOM algorithm, and the stability dynamics of these vortex solitons are studied by the linear stability spectra and nonlinear evolution of the model.

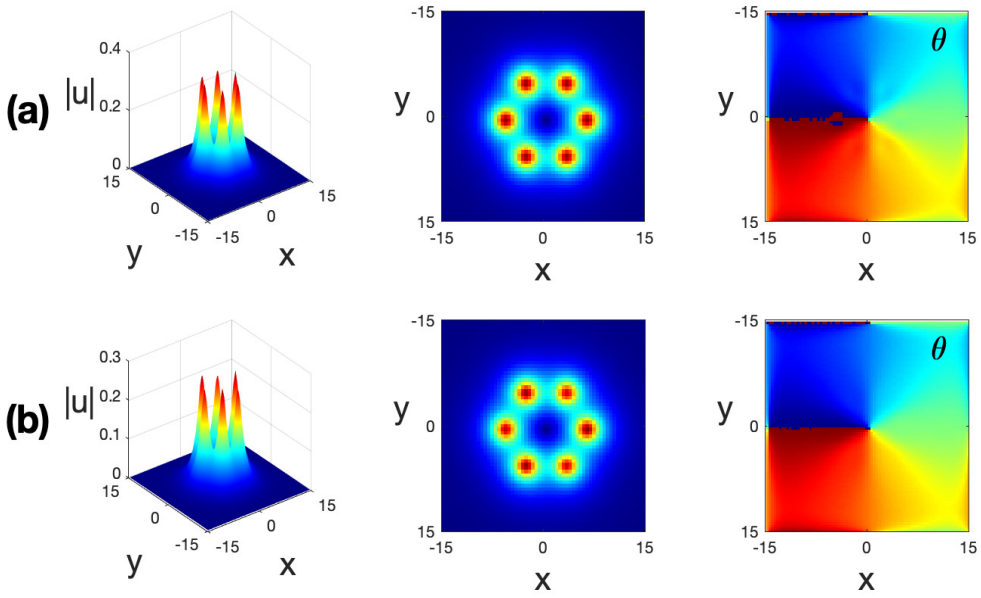

Figure 2.2: 3D profile, top view and phase structure of the six-hump vortex solitons located at local maxima of the azimuthal potential for the parameters given in (2.3) (a) when $\sigma = 1$ (the first row); (b) when $\sigma = -1$ (the second row). $c = 2$, $\Delta t = 0.2$ and vorticity $m = 1$ in both cases.

3.1. Linear stability analysis

The model (2.1) is linearized to calculate linear spectrum of vortex solitons as follows. By denoting

$$U = e^{i\mu z}[u_0(x,y) + g(x,y)e^{\lambda z} + h^*(x,y)e^{\lambda^* z}]$$

where $u_0(x,y)$ is the vortex soliton and $g,h \ll 1$ are perturbed infinitesimal modes. Inserting the perturbed solution U into the model (2.1), the following eigenvalue problem is obtained

$$\mathscr{L}\mathbf{V} = \lambda\mathbf{V}$$

where

$$\mathscr{L} = i\begin{pmatrix} \mathscr{L}_{11} & \mathscr{L}_{12} \\ \mathscr{L}_{21} & \mathscr{L}_{22} \end{pmatrix}, \quad \mathbf{V} = \begin{pmatrix} g \\ h \end{pmatrix}$$

and the matrix coefficients of $\mathscr{L}$ are

$$\begin{aligned} \mathscr{L}_{11} &= \Delta - \mu - \rho\phi + V, \\ \mathscr{L}_{12} &= u^2, \\ \mathscr{L}_{21} &= -(u^2)^*, \\ \mathscr{L}_{22} &= -(\Delta - \mu - \rho\phi + V)^*. \end{aligned}$$

The eigenvalues of $\mathscr{L}$ can be calculated numerically by the Fourier collocation method [35]. If any eigenvalue in the spectrum has a positive real part, the solution is linearly unstable.

The power of solitons, that is calculated by P=$\iint_{-\infty}^{\infty}|u|^2dxdy$, plays an important role in the stability analysis. Therefore, the power-eigenvalue diagram of gap solitons are investigated in Figure 3.1(a), and stability properties of considered vortex solitons are investigated in Figure 3.1(b) for the same parameters. Blue line shows p$\mathscr{PT}$-symmetric ($\sigma = 1$) and red line shows $\mathscr{PT}$-symmetric ($\sigma = -1$) case of the azimuthal potential. In Figure 3.1(a), the linear stability (solid line) and instability (dotted) regions are determined by computation of eigenvalue spectra for each point on the power curves and the maximum real parts of these spectra are given in Figure 3.1(b). From the power-eigenvalue ($P - \mu$) diagram, it can be seen that the vortices are linearly stable below a critical power $P_c = 4.14$, that corresponds to $\mu = 0.58$, in both $\sigma = 1$ and $\sigma = -1$ cases when $p_{re} = 6$ and $p_{im} = 1$ (see Figure 3.1(a)).

Similarly, the power and stability properties of vortex solitons are shown in Figure 3.2 for the parameters ρ, ν, p_{re} and p_{im}. It is important to note that this analysis shows the first band-gap boundaries for the considered parameter regimes in each panel. For instance, when $\nu = 1.5$, $p_{re} = 6$, $p_{im} = 1$, $\mu = 0.5$ and $\sigma = 1$, the vortex solitons can be obtained for $\rho \in [0, 1.85]$ within the gap region (see blue line in Figure 3.2(a)). It is observed that, although linear stability region for the anisotropy coefficient ν and potential depth of real part p_{re} are identical in both $\sigma = 1$ and $\sigma = -1$ cases, stability region of p$\mathscr{PT}$-symmetric ($\sigma = 1$) lattice is larger than that of $\mathscr{PT}$-symmetric ($\sigma = -1$) lattice for the coupling parameter ρ and potential depth of imaginary part p_{im}.

The vortex solitons that are shown in Figure 2.2(a) and 2.2(b) correspond to 'a' and 'b' points in Figure 3.2(d), respectively. This fact reveals the linear stability of the vortices at point 'a' and 'b' when $\sigma = 1$ and $\sigma = -1$.

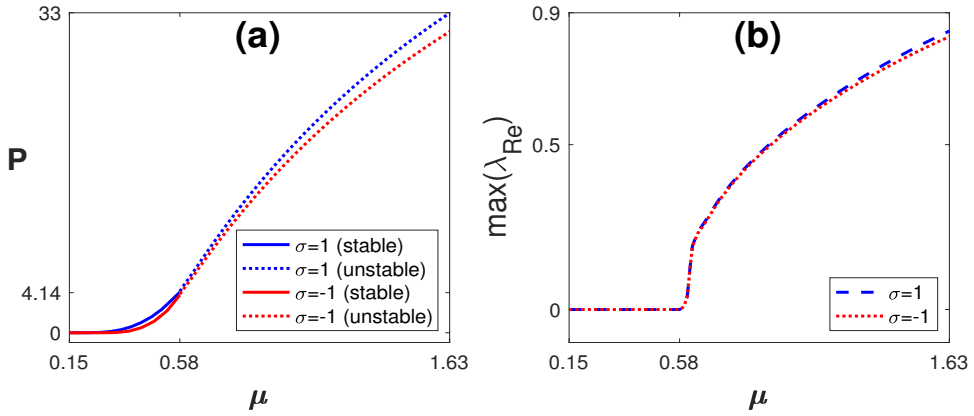

Figure 3.1: The power of vortex solitons versus eigenvalue (a) and the maximum real part in the eigenvalue spectrum (b) for varied values of μ when $\rho = 0.5$, $\nu = 1.5$, $p_{re} = 6$ and $p_{im} = 1$.

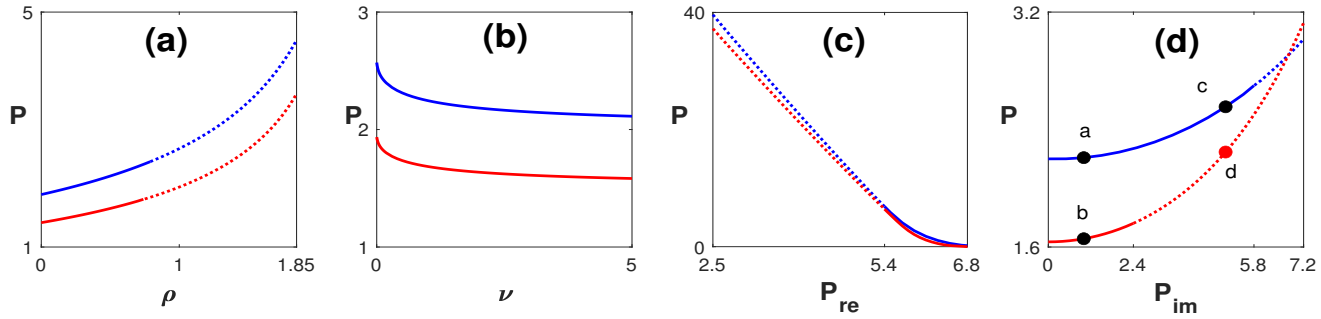

Figure 3.2: The power of vortex solitons (a) for varied values of ρ when $\nu = 1.5$, $p_{re} = 6$, $p_{im} = 1$ and $\mu = 0.5$; (b) for varied values of ν when $\rho = 0.5$, $p_{re} = 6$, $p_{im} = 1$ and $\mu = 0.5$; (c) for varied values of p_{re} when $\rho = 0.5$, $\nu = 1.5$, $p_{im} = 1$ and $\mu = 0.5$; (d) for varied values of p_{im} when $\rho = 0.5$, $\nu = 1.5$, $p_{re} = 6$ and $\mu = 0.5$. Blue line shows p$\mathscr{P}\mathscr{T}$-symmetric ($\sigma = 1$) and red line shows $\mathscr{P}\mathscr{T}$-symmetric ($\sigma = -1$) case of the azimuthal potential where solid and dotted line show stable and unstable regions for the gap solitons, respectively.

3.2. Nonlinear evolution of vortex solitons

To test the full stability, the nonlinear stability of vortex solitons are investigated by direct simulation of the model (2.1) for long times. A finite-difference discretization scheme is used in the spatial domain and the solution is advanced in z with a fourth-order Runge-Kutta method. The initial condition of evolution is taken to be a vortex structure that is obtained by the SOM algorithm and perturbed with 1% random noise in amplitude and phase.

Linear stability spectra and nonlinear evolution of the vortices, that are obtained at 'a', 'b', 'c' and 'd' points in Figure 3.2(d), are examined in columns (a), (b), (c) and (d) of Figure 3.3, respectively. The nonlinear evolution of perturbed vortices (the first row), linear stability spectra (the second row) and 3D view of the evolved vortex profiles (the third row) are shown in Figure 3.3. As can be seen from Figure 3.3(a), 3.3(b) and 3.3(c), the linear spectra of vortex solitons that are obtained at 'a', 'b', 'c' points are purely-imaginary (none of their eigenvalues have a real part), the peak amplitude of the evolved vortices oscillate relatively small amplitudes during the propagation, and vortex profiles are preserved after evolution at $z = 500$, thus stable evolution of the vortex structures can be achieved for the considered parameter regimes. On the other hand, the linear spectrum of the vortex solitons, that is obtained at point 'd', involves eigenvalues with positive real parts, peak amplitude of the evolved soliton increases significantly during the evolution and the vortex profile breaks up after evolution at $z = 500$ (see Figure 3.3(d)). These facts indicate the instability of vortex structure due to blow-up of solitons when $\sigma = -1, p_{re} = 6$ and $p_{im} = 5$.

It should be noted that the result of nonlinear evolution analysis is consistent with linear (in)stability regions that are given in Figure 3.2 for the $\mathscr{P}\mathscr{T}$-symmetric and p$\mathscr{P}\mathscr{T}$-symmetric azimuthal lattices. To see the impact of quadratic optical effects and depth of p$\mathscr{P}\mathscr{T}$-symmetric azimuthal lattices on the pulse stability, the evolution of peak amplitudes are examined for varied ρ, ν, p_{re} and p_{im} values in Figure 3.4. Here, the initial condition is chosen as the vortex at point 'd' that is shown to be nonlinearly unstable in Figure 3.3(d), and the initial peak amplitude of the vortex solitons are normalized to 1 for comparison. The results in Figure 3.4 show that, by increasing the value of optical rectification parameter ρ and lattice depth of the imaginary part p_{im}, peak amplitude of vortices are increasing more rapidly, and thus collapse of vortices are accelerated (see panels (a) and (d)). Conversely, the increase in peak amplitude can be delayed by increasing anisotropy parameter ν and lattice depth of the real part p_{re} (see panels (b) and (c)). These results consistent with previous studies that have demonstrated stability of two dimensional solitons that are generated by the NLSM system with periodic [31], quasi-periodic [32] and p$\mathscr{P}\mathscr{T}$-symmetric [33] lattices. In [31], it was also shown that, collapse will eventually occur in a lattice-free NLSM system, and collapse of the solitons are expedited by increasing values of ρ and ν in the lattice-free medium.

It should be noted that, although vortex solitons can be obtained in semi-infinite interval when $\nu > 0$ and increased values of ν assists maintaining the peak amplitude of the vortices in the p$\mathscr{P}\mathscr{T}$-symmetric azimuthal lattices, it can not be considered as a collapse arrest mechanism, since ρ and ν parameters are prescribed coefficients that are depending on the type of optical materials.

In addition, it is observed that, as shown in [21], there is different stability properties of vortices for different vorticity values that is denoted by m in equation (2.2) and fixed to 1 in the study. Linear stability spectra and peak amplitudes of the evolved vortices are displayed in Figure 3.5 for $m = +1$ and $m = -1$ when $\rho = 1, \nu = 1.5, p_{re} = 6, p_{im} = 1$ and $\mu = 1$. As can be seen from Figure 3.5, although the linear stability spectra and nonlinear evolution of the vortices are overlapping for the $\mathscr{P}\mathscr{T}$-symmetric lattice ($\sigma = -1$) (see the second row (b)),

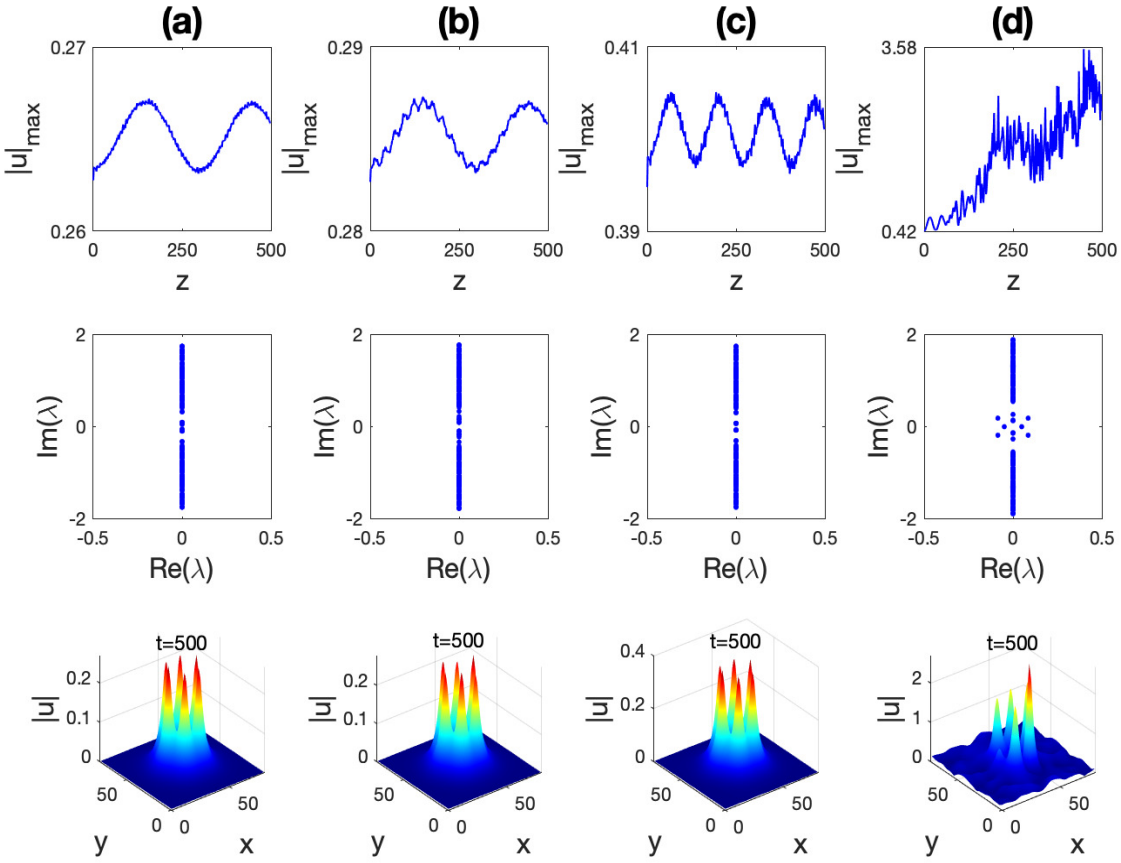

Figure 3.3: The peak amplitude of evolved vortices from $z = 0$ to $z = 500$ (the first row), linear stability spectra (the second row) and 3D view of vortex profile after evolution at $z = 500$ (the third row). The vortex solitons are generated (a) when $\sigma = 1$, $p_{re} = 6$ and $p_{im} = 1$; (b) when $\sigma = -1$, $p_{re} = 6$ and $p_{im} = 1$; (c) when $\sigma = 1$, $p_{re} = 6$ and $p_{im} = 5$; (d) when $\sigma = -1$, $p_{re} = 6$ and $p_{im} = 5$. $\rho = 0.5$, $\nu = 1.5$ and $\mu = 0.5$ in all cases.

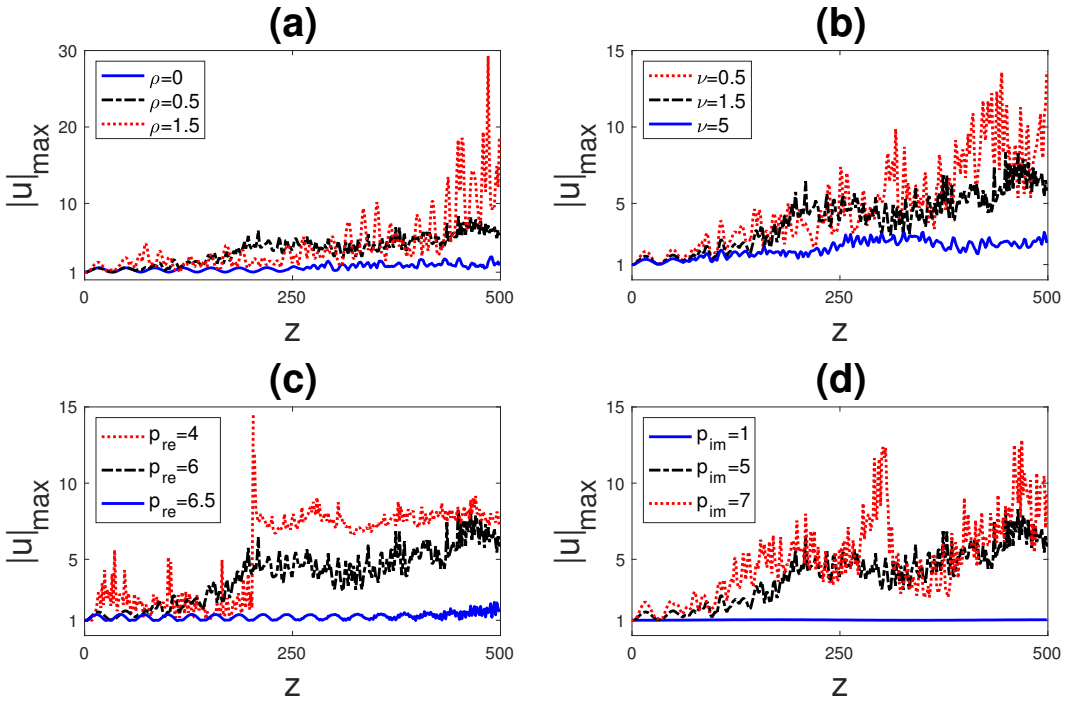

Figure 3.4: The peak amplitude of the evolved vortices in the p$\mathscr{P}\mathscr{T}$-symmetric azimuthal potential. The vortex is obtained (a) for varied values of ρ when $\nu = 1.5$, $p_{re} = 6$ and $p_{im} = 5$; (b) for varied values of ν when $\rho = 0.5$, $p_{re} = 6$ and $p_{im} = 5$; (c) for varied values of p_{re} when $\rho = 0.5, \nu = 1.5$ and $p_{im} = 5$; and (d) for varied values of p_{im} when when $\rho = 0.5, \nu = 1.5$ and $p_{re} = 6$. $\mu = 0.5$ in all cases.

the stability spectra and nonlinear evolution of the vortices are different for the p$\mathscr{P}\mathscr{T}$-symmetric lattice ($\sigma = 1$) (see the first row (a)). The maximum real part in the linear stability spectrum for $m = +1$ is larger than that for $m = -1$ when $\sigma = -1$ (see left panel in Figure 3.5(a)).

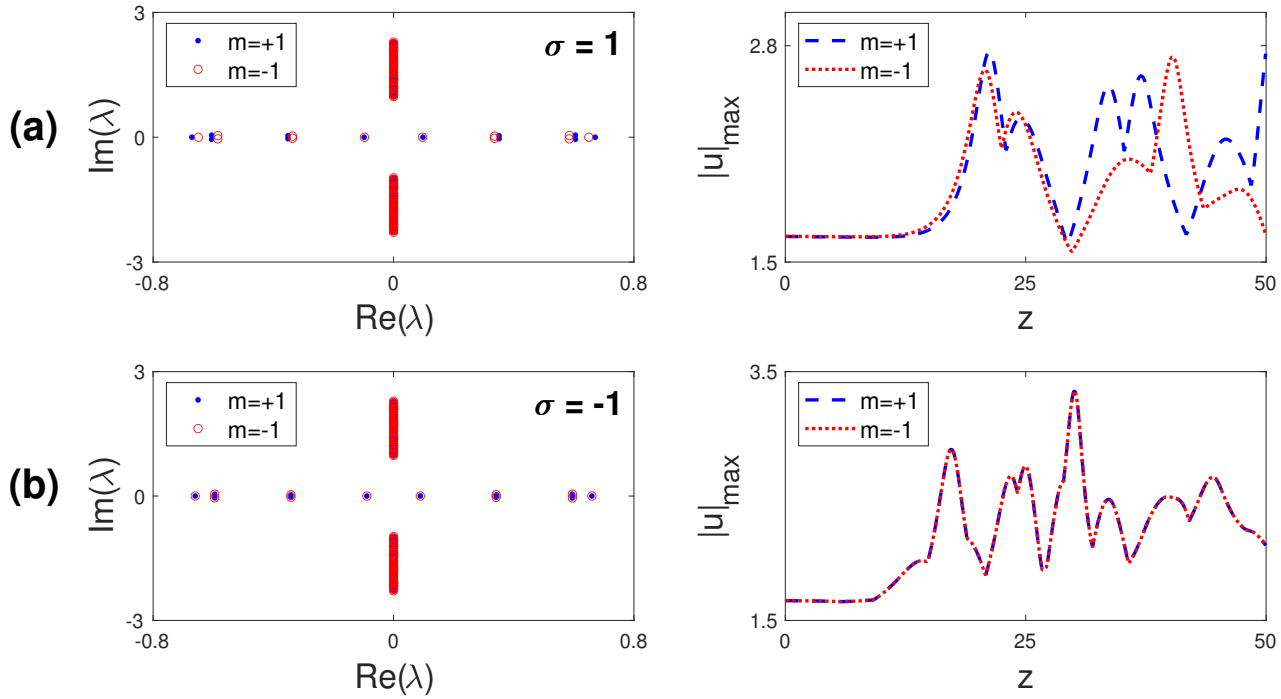

Figure 3.5: The linear stability spectra (the first column) and peak amplitude of evolved vortices from $z = 0$ to $z = 50$ (the second column) for $m = +1$ and $m = -1$. The vortex solitons are generated when $\rho = 1, \nu = 1.5, p_{re} = 6, p_{im} = 1$ and $\mu = 1$ (a) for the p$\mathscr{P}\mathscr{T}$-symmetric lattice ($\sigma = 1$); (b) for the $\mathscr{P}\mathscr{T}$-symmetric lattice ($\sigma = -1$)

In order to support this result, the maximum real part in the spectrum versus eigenvalue(μ) is depicted in Figure 3.6 for $m = +1$ and $m = -1$. It is shown that the difference between the maximum real parts in the spectra are increasing with increasing values of μ for the examined

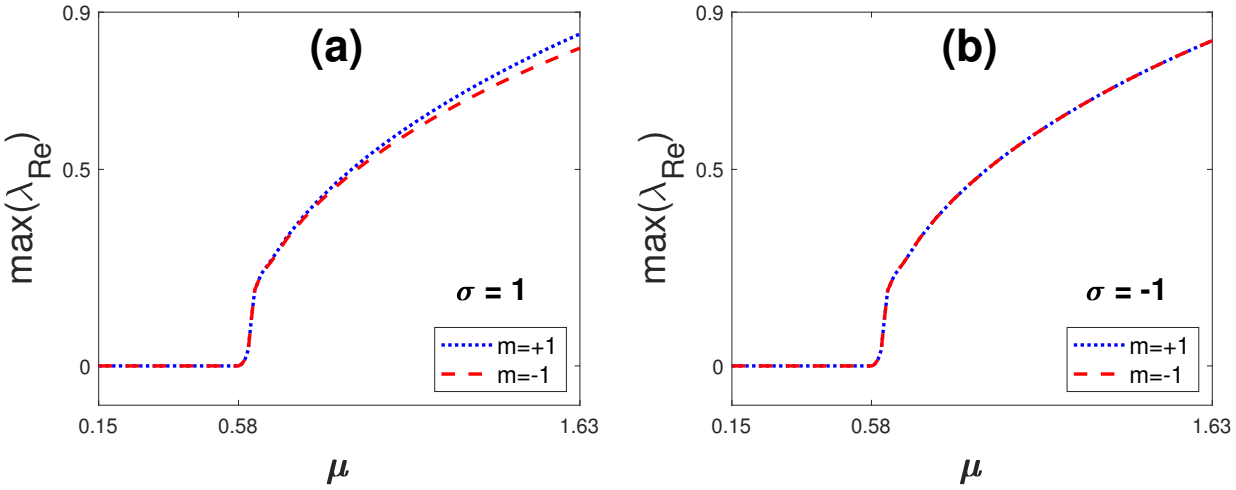

Figure 3.6: The maximum real part in the spectrum versus propagation constant (μ) for $m = +1$ and $m = -1$ (a) when $\sigma = 1$; (b) when $\sigma = -1$. $\rho = 0.5$, $\nu = 1.5$, $p_{re} = 6$ and $p_{im} = 1$ in all cases.

vorticity values ($m = +1$ and $m = -1$) in the p$\mathscr{P}\mathscr{T}$-symmetric lattice (see panel (a)). In contrast, no such difference is observed in the $\mathscr{P}\mathscr{T}$-symmetric lattice for different vorticity values (see panel (b)).

4. Conclusions

The numerical existence of vortex solitons in $\mathscr{P}\mathscr{T}$-symmetric ($\sigma = -1$) and p$\mathscr{P}\mathscr{T}$-symmetric ($\sigma = 1$) azimuthal potentials are demonstrated for the quadratic nonlinear media, and stability properties in the considered lattices are explored by examining the nonlinear evolution and linear stability spectra of the vortex structures. It has been shown that, although the existence domain of the $\mathscr{P}\mathscr{T}$-symmetric and p$\mathscr{P}\mathscr{T}$-symmetric lattices are identical, the stability region of $\mathscr{P}\mathscr{T}$-symmetric lattice is narrower than that of the p$\mathscr{P}\mathscr{T}$-symmetric lattice. Linear stability spectra and nonlinear evolution of vortices show that, the stable evolution of vortex structures can be achieved in both $\mathscr{P}\mathscr{T}$-symmetric and p$\mathscr{P}\mathscr{T}$-symmetric azimuthal potentials for a wide range of parameters, and although there is a threshold value of the depth of imaginary part in the $\mathscr{P}\mathscr{T}$-symmetric potential for the stability of vortices, there is not any phase-transition point for the

p$\mathscr{PT}$-symmetric potential. Accordingly, it is demonstrated that stable vortex structures can exist in p$\mathscr{PT}$-symmetric potentials, where the symmetry is already broken in the $\mathscr{PT}$-symmetric counterpart of the potential.
Moreover, it has been observed that there are different stability properties of vortices in p$\mathscr{PT}$-symmetric azimuthal potentials for different vorticity values, while there is no such difference for vortices in $\mathscr{PT}$-symmetric potentials.
Linear stability spectra together with the nonlinear evolution reveal that deeper real part in the azimuthal potentials support stability of vortices, whereas deeper imaginary part and strong quadratic electro-optic effects in the medium impoverish stability properties of the vortices.

Acknowledgements

The authors would like to express their sincere thanks to the editor and the anonymous reviewers for their helpful comments and suggestions.

Funding

There is no funding for this work.

Availability of data and materials

Not applicable.

Competing interests

The authors declare that they have no competing interests.

Authors' contributions

All authors contributed equally to the writing of this paper. All authors read and approved the final manuscript.

References

[1] M. J. Ablowitz, N. Antar, İ. Bakırtaş, B. Ilan, *Band-gap boundaries and fundamental solitons in complex two-dimensional nonlinear lattices*, Phys. Rev. A., **81**(3) (2010), 033834.
[2] M. J. Ablowitz, N. Antar, İ. Bakırtaş, B. Ilan, *Vortex and dipole solitons in complex two-dimensional nonlinear lattices*, Phys. Rev. A., **86**(3) (2012), 033804.
[3] M. J. Ablowitz, B. Ilan, E. Schonbrun, R. Piestun, *Solitons in two-dimensional lattices possessing defects, dislocations, and quasicrystal structures*, Phys. Rev. E., **74**(3) (2006), 035601.
[4] G. Burlak, B. A. Malomed, *Matter-wave solitons with the minimum number of particles in two-dimensional quasiperiodic potentials*, Phys. Rev. E., **85**(5) (2012), 057601.
[5] M. Bağcı, İ. Bakırtaş, N. Antar, *Vortex and dipole solitons in lattices possessing defects and dislocations*, Opt. Commun., **331** (2014), 204-218.
[6] J. Yang, *Necessity of pt symmetry for soliton families in one-dimensional complex potentials*, Phys. Lett. A., **378**(4) (2014), 367-373.
[7] D. N. Christodoulides, J. Yang, *Parity-Time Symmetry and Its Applications*, Singapore, Springer, 2018.
[8] C. M. Bender, S. Boettcher, *Real spectra in non-hermitian hamiltonians having PT symmetry*, Phys. Rev. Lett., **80**(24) (1998), 5243-5246.
[9] K. G. Makris, R. El-Ganainy, D. N. Christodoulides, Z. H. Musslimani, *Beam dynamics in PT symmetric optical lattices*, Phys. Rev. Lett., **100**(10) (2008), 103904.
[10] C. E. Rüter, K. G. Makris, R. El-Ganainy, D. N. Christodoulides, M. Segev, D. Kip, *Observation of parity-time symmetry in optics*, Nat. Phys., **6**(3) (2010), 192-195.
[11] A. Regensburger, C. Bersch, M. A. Miri, G. Onishchukov, D. N. Christodoulides, U. Peschel, *Parity-time synthetic photonic lattices*, Nature, **488** (2012), 167-171.
[12] L. Feng, R. El-Ganainy, L. Ge, *Non-hermitian photonics based on parity-time symmetry*, Nat. Photon, **11**(12) (2017), 752-762.
[13] J. Yang, *Symmetry breaking of solitons in one-dimensional parity-time-symmetric optical potentials*, Opt. Lett., **39**(19) (2014), 5547-5550.
[14] İ. Göksel, N. Antar, İ. Bakırtaş, *Solitons of (1+1)d cubic-quintic nonlinear Schrödinger equation with pt-symmetric potentials*, Opt. Commun., **354** (2015), 277-285.
[15] Q. Zhou,, A. Biswas, *Optical solitons in parity-time-symmetric mixed linear and nonlinear lattice with non-Kerr law nonlinearity*, Superlattices and Microstructures, **109** (2017), 588-598.
[16] M. Bağcı, İ. Bakırtaş, N. Antar, *Fundamental solitons in parity-time symmetric lattice with a vacancy defect*, Opt. Commun., **356** (2015), 472-481.
[17] İ. Göksel, N. Antar, İ. Bakırtaş, *Two-dimensional solitons in PT-symmetric optical media with competing nonlinearity*, Optik., **156** (2018), 470-478.
[18] İ. Göksel, N. Antar, İ. Bakırtaş, *Two-dimensional solitons in cubic-saturable media with PT-symmetric lattices*, Chaos Solitons Fractals., **109** (2018), 83-89
[19] J. Yang, *Symmetry breaking of solitons in two-dimensional complex potentials*, Phys. Rev. E., **91**(2) (2015), 023201.
[20] J. Yang, *Partially PT symmetric optical potentials with all-real spectra and soliton families in multidimensions*, Opt. Lett., **39**(5) (2014), 1133-1136.
[21] Y. V. Kartashov, V. V. Konotop, L. Torner, *Topological states in partially-PT -symmetric azimuthal potentials*, Phys. Rev. Lett., **115**(19) (2015), 193902.
[22] L. C. Crasovan, J. P. Torres, D. Mihalache, L. Torner, *Arresting wave collapse by wave self- rectification*, Phys. Rev. Lett., **91**(6) (2003), 063904.
[23] R. Schiek, T. Pertsch,*Absolute measurement of the quadratic nonlinear susceptibility of lithium niobate in waveguides*, Opt. Mater. Express., **2**(2) (2012), 126-139.
[24] M. J. Ablowitz, G. Biondini, S. Blair, *Localized multi-dimensional optical pulses in non-resonant quadratic materials*, Math. Comput. Simul., **56** (2001), 511-519.
[25] M. Bağcı, J. N. Kutz, *Spatiotemporal mode locking in quadratic nonlinear media*, Phys. Rev. E., **102**(2) (2020), 022205.
[26] D. J. Benney, G. J. Roskes, *Wave instabilities*, Stud. in App. Math., **48** (1969), 377-385.
[27] A. Davey, K. Stewartson, *On three-dimensional packets of surface waves*, Proc. of the Royal Soc. of London. Series A, Math. and Phys. Sci., **338** (1974), 101-110.
[28] M. J. Ablowitz, G. Biondini, S. Blair, *Multi- dimensional pulse propagation in non-resonant $\chi^{(2)}$ materials*, Phys.Lett. A., **236**(5) (1997), 520-524.
[29] M. J. Ablowitz, G. Biondini, S. Blair, *Nonlinear Schrödinger equations with mean terms in nonresonant multidimensional quadratic materials*, Phys. Rev. E., **63**(4) (2001), 046605.
[30] M. J. Ablowitz, İ. Bakırtaş, B. Ilan, *Wave collapse in a class of nonlocal nonlinear Schrödinger equations*, Physica D: Nonlinear Phenomena, **207**(3) (2005), 230-253.
[31] M. Bağcı, İ. Bakırtaş, N. Antar, *Lattice solitons in nonlinear Schrödinger equation with coupling-to-a-mean-term*, Opt. Commun., **383** (2017), 330-340.

[32] M. Bağcı, *Soliton dynamics in quadratic nonlinear media with two-dimensional pythagorean aperiodic lattices*, J. Opt. Soc. Am. B., **38**(4) (2021), 1276-1282.
[33] M. Bağcı, *Partially PT -symmetric lattice solitons in quadratic nonlinear media*, Phys. Rev. A., **103**(2) (2021), 023530.
[34] J. Yang, T. I. Lakoba, *Universally-convergent squared-operator iteration methods for solitary waves in general nonlinear wave equations*, Stud. in App. Math., **118**(2) (2007), 153-197.
[35] J. Yang, *Nonlinear Waves in Integrable and Nonintegrable Systems*, SIAM, Philadelphia, 2010.

Journal of Mathematical Sciences and Modelling, 4 (3) (2021) 126-132
Research Article

Journal of Mathematical Sciences and Modelling

Journal Homepage: www.dergipark.gov.tr/jmsm
ISSN 2636-8692
DOI: http://dx.doi.org/10.33187/jmsm.1022320

New wave behaviors of the (3+1)-dimensional Date-Jimbo-Kashiwara-Miwa equation

S. Şule Şener Kılıç[1]

[1]*Department of mathematics, Faculty of Science, Ataturk University, 25240, Erzurum, Turkey*

Article Info

Keywords: *(3+1)-dimensional Date-Jimbo-Kashiwara-Miwa equation, generalized exponential rational function method, exact solutions*
2010 AMS: *35Q99, 35Q92.*
Received: *11 November 2021*
Accepted: *21 December 2021*
Available online: *29 December 2021*

Abstract

In this study, the (3+1)-dimensional Date-Jimbo-Kashiwara-Miwa equation that indicated the propagation of nonlinear dispersive waves in inhomogeneous media is given for consideration. The generalized exponential rational function method is used to seek some new exact solutions for the considered equation. The three-dimensional surfaces and two-dimensional graphs of the obtained solutions are plotted by choosing the appropriate values of the involving free parameters.

1. Introduction

Nonlinear partial differential equations (NPDEs) are frequently employed to subedit real-world issues from a mathematical standpoint. There are several situations in which simulations of these instances are necessary. These important areas include fiber optics, fluid mechanics, electromagnetic theory, plasma physics, nuclear physics, mass transport, hydrodynamics, population and economics, and many more [1–10]. As a consequence, exact analytic solutions to such equations become the most important factor to consider, because they can supply important data for accurate explanations of natural processes. Many academics and mathematicians have worked hard over the last few decades to find explicit solutions to NPDEs. For this aim, many analytical methods have been created to obtain such exact solutions like sin-Gordon expansion method [11–14], the $(1/G')$ −expansion method [15–17], the simplified Hirota's method [18–20], the Backlund transformation method [21, 22], and symbolic computational method [23].
The (2+1)-dimensional Date-Jimbo-Kashiwara-Miwa (DJKM) reads [24–26]

$$Q_{xxxxy}+4Q_{xxy}Q_x+2Q_{xxx}Q_y+6Q_{xy}Q_{xx}-\alpha Q_{yyy}-2\beta Q_{xxt}=0, \tag{1.1}$$

where α and β are real constants, $Q(x,y,t)$ indicated the wave's maximum extension as evaluated from its equilibrium state. Eq. (1.1) represents the propagation of nonlinear dispersive waves in inhomogeneous media. The DJKM equation was first developed by Date et al. [24]. In [27], Wazwaz has developed the (2+1) dimensional DJKM equation to a new (3+1)-dimensional DJKM equation by adding the term $\left(kQ_x+rQ_y+sQ_z\right)_{xx}$ which is given by

$$Q_{xxxxy}+4Q_{xxy}Q_x+2Q_{xxx}Q_y+6Q_{xy}Q_{xx}-\alpha Q_{yyy}-2\beta Q_{xxt}+\left(kQ_x+rQ_y+sQ_z\right)_{xx}=0. \tag{1.2}$$

Wazwaz demonstrated that Eq. (1.2) is a completely integrable equation via using the Painlevé test, and used Hirota's simple method to construct multiple soliton solutions as well as solitonic, singular, and periodic solutions. In [28], the authors used three analytical methods namely the $\exp(-\phi(\xi))-$ expansion method, the $(G'/G)-$ expansion method, and the sine-Gordon expansion method to Eq. (1.2), as a result, several exact solutions have been obtained. Furthermore, they used the finite difference method to attain some numerical solutions. In this paper, we will use the generalized exponential rational function method (GERFM) to construct some new exact solutions to the (3+1)-dimensional DJKM equation.

Email addresses and ORCID numbers: senersule@atauni.edu.tr, 0000-0002-3807-7105 (S. Ş. Ş. Kılıç)

2. Description of the method

In this section, the basic concepts of the GERFM [29–32] are given:
Step 1: Consider the general form of NPDE as

$$\Psi\left(Q(x,y,z,t),Q_x,Q_y,Q_z,Q_t,Q_{xt},Q_{xx},Q_{yt},Q_{yy},...\right)=0. \tag{2.1}$$

Let us take the wave transformation as follows:

$$Q(x,y,z,t)=\psi(\varsigma),\ \varsigma=ax+by+dz-ct, \tag{2.2}$$

where a,b,d, and c are constants to be calculated. Using Eq. (2.2) into Eq. (2.1), we get the following nonlinear ordinary differential equation:

$$\Theta\left(\psi,\psi',\psi'',\psi''',...\right)=0. \tag{2.3}$$

Step 2: Let the solution of Eq. (2.3) have the following form

$$\psi(\varsigma)=a_0+\sum_{j=1}^{N}a_j\phi(\varsigma)^j+\sum_{j=1}^{N}b_j\phi(\varsigma)^{-j}, \tag{2.4}$$

where

$$\phi(\varsigma)=\frac{\gamma_1e^{\lambda_1\varsigma}+\gamma_2e^{\lambda_2\varsigma}}{\gamma_3e^{\lambda_3\varsigma}+\gamma_4e^{\lambda_4\varsigma}}, \tag{2.5}$$

where $\lambda_m,\gamma_m\ (1\leq m\leq 4)$ are real/complex constants, a_0,a_j,b_j are constants to be calculated, N will be found by balance principle.
Step3: Inserting Eq. (2.5) in Eq. (2.4) then using Eq. (2.4) in Eq. (2.3), then we get a polynomial which is dependent on Eq. (2.5). By setting the like order terms equal to zero, we achieve a system of algebraic equations concerning a,b,c,d,a_0,a_1, and b_1. Solving the obtained system with the aid of any symbolic computation software, the values of the involved parameters will be determined and replacing the determined values into Eq. (2.3), one may obtain the solutions of Eq. (2.1).

3. Applications of model

In this section, we apply the GERFM to Eq.(1.2). Firstly, by inserting Eq. (2.2) into Eq.(1.2), we get

$$6a^3b\psi''(\varsigma)^2+\left(a^3k-b^3\alpha+a^2(br+ds+2c\beta)+6a^3b\psi'(\varsigma)\right)\psi'''(\varsigma)+a^4b\psi''''(\varsigma)=0. \tag{3.1}$$

Inserting Eq. (3.1) twice, and set the constants of integration to zero, so one may get

$$3a^3b\psi'(\varsigma)^2+\left(a^3k-b^3\alpha+a^2(br+ds+2c\beta)\psi'(\varsigma)\right)+a^4b\psi'''(\varsigma)=0.$$

Using the balance principle between the term $\psi'''(\varsigma)$ and $\psi'(\varsigma)^2$, we have $N=1$. Considering Eq. (2.4) with $N=1$, then it takes the below form

$$\psi(\varsigma)=a_0+a_1\phi(\varsigma)+\frac{b_1}{\phi(\varsigma)}. \tag{3.2}$$

In what follows, different solitary wave solutions are constructed under certain conditions
Family 1: Using $\gamma=\{-2,-1,1,1\}$, $\lambda=\{0,1,0,1\}$ in Eq. (2.5), then one may have

$$\phi(\varsigma)=\frac{-2-e^{\varsigma}}{1+e^{\varsigma}}.$$

Case 1: $k=\frac{b^3\alpha}{a^3},c=-\frac{b\left(a^2+r\right)+ds}{2\beta},a_1=2a,b_1=0.$

$$\psi_1(\varsigma)=a_0+\frac{2a(-2-e^{\varsigma})}{1+e^{\varsigma}}.$$

Then, one may have an exact solution of the exponential type

$$Q_1(x,y,z,t)=a_0+\frac{2a\left(-2-e^{ax+by+dz+\frac{\left(b\left(a^2+r\right)+ds\right)t}{2\beta}}\right)}{1+e^{ax+by+dz+\frac{\left(b\left(a^2+r\right)+ds\right)t}{2\beta}}}. \tag{3.3}$$

Family 2: $\gamma=\{-2-i,2-i,-1,1\},\lambda=\{i,-i,i,-i\}$ into Eq. (2.5), then one may have

$$\phi(\varsigma)=\frac{\cos(\varsigma)+2\sin(\varsigma)}{\sin(\varsigma)}.$$

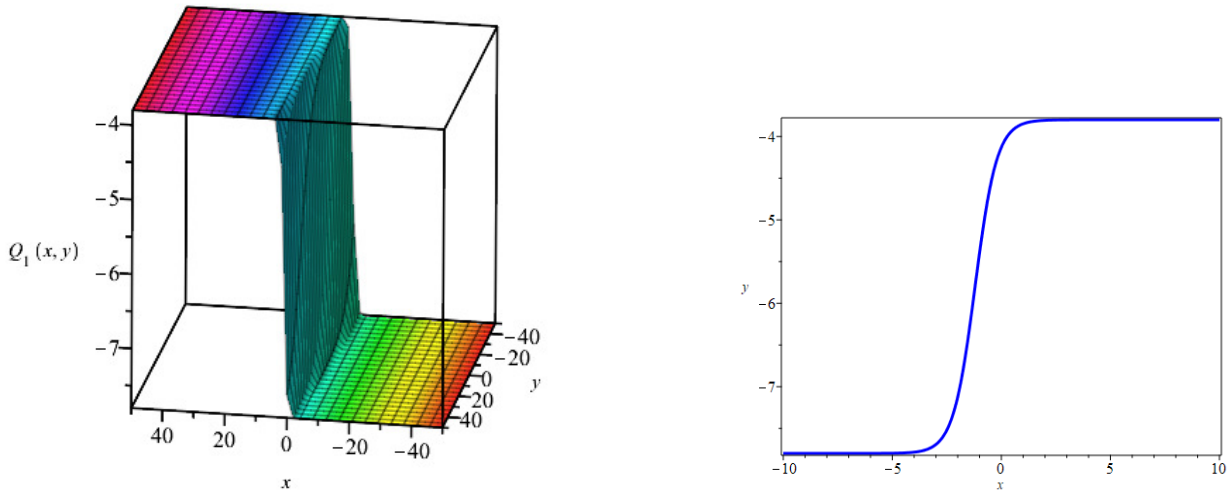

Figure 3.1: 3D dimensional surface and 2D graphs of solution of Eq. (3.3) where $y=1, z=1, t=1, a=2, a_0=0.2, b=-0.1, d=0.01, s=0.01, \beta=-0.1$, and $r=1$.

Case 1: $k=\frac{b^3\alpha}{a^3}, d=\frac{4a^2b-br-2c\beta}{s}, b_1=-10a, a_1=0.$

$$\psi_2(\varsigma)=a_0-\frac{10a\sin(\varsigma)}{\cos(\varsigma)+2\sin(\varsigma)}.$$

So, we have a trigonometric type solution as below

$$Q_2(x,y,z,t)=a_0+\frac{10a\sin\left(ct-ax-by-\frac{z\left(4a^2b-br-2c\beta\right)}{s}\right)}{\cos\left(ct-ax-by-\frac{z(4a^2b-br-2c\beta)}{s}\right)-2\sin\left(ct-ax-by-\frac{z(4a^2b-br-2c\beta)}{s}\right)}. \tag{3.4}$$

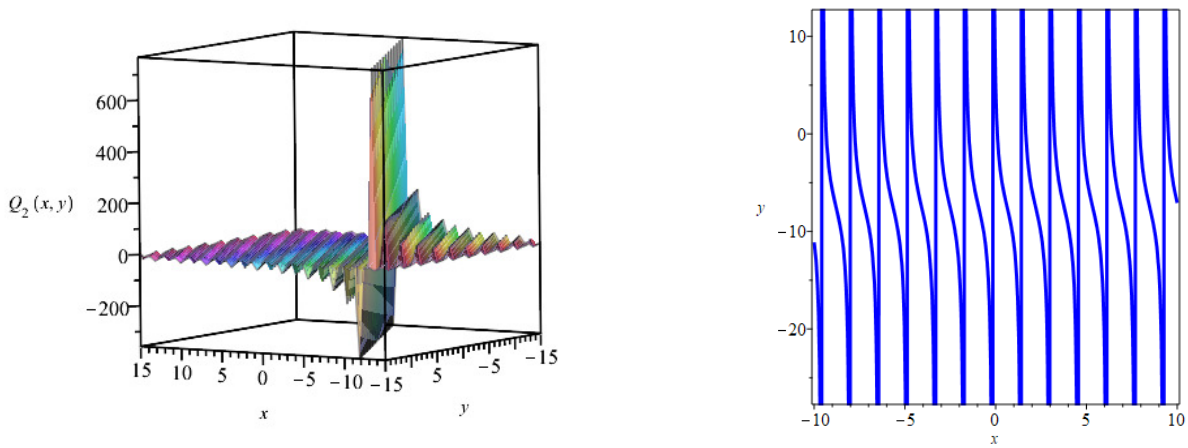

Figure 3.2: 3D dimensional surface and 2D graphs of solution of Eq. (3.4) for values of $\alpha=0.2, a=2, c=3, b=1, r=2, \beta=0.3, s=3/2, a_0=0.5, t=1, z=1$, and $y=1$.

Family 3: Using $\gamma=\{2,0,1,1\}, \lambda=\{-1,0,1,-1\}$ in Eq. (2.5), so it takes the following form

$$\phi(\varsigma)=\frac{\cosh(\varsigma)-\sinh(\varsigma)}{\cosh(\varsigma)}. \tag{3.5}$$

Case 1: Plugging these results in with Eq. (3.5) into Eq. (3.2), we get

$$\psi_3(\varsigma)=a_0-2asech(\varsigma)(\cosh(\varsigma)-\sinh(\varsigma)).$$

Then, one may have a solution of hyperbolic type as follows

$$Q_3(x,y,z,t)=a_0-2asech(ct-ax-by-dz)(\cosh(ct-ax-by-dz)+\sinh(ct-ax-by-dz)). \tag{3.6}$$

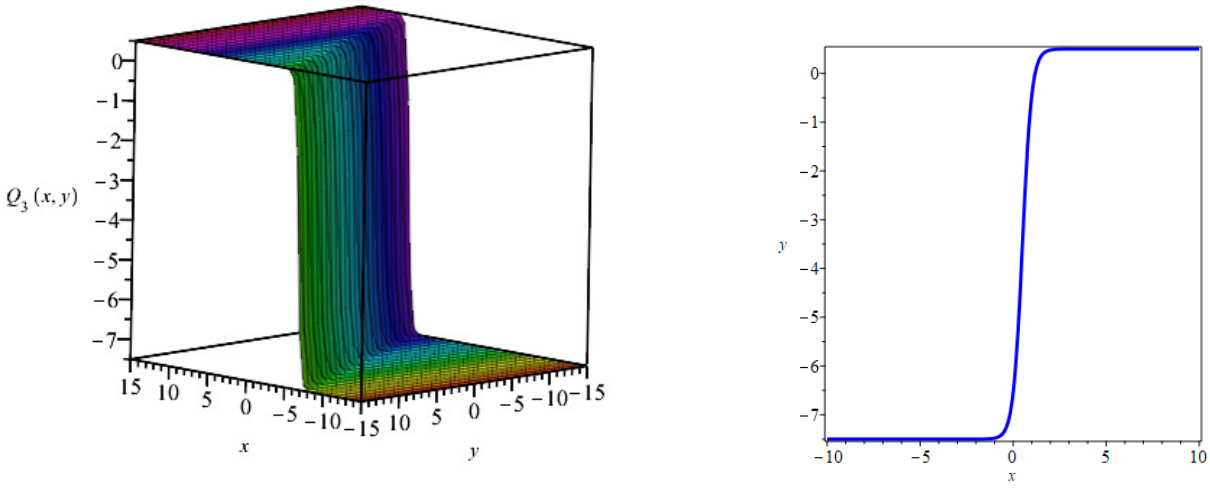

Figure 3.3: 3D dimensional surface and 2D graphs of solution of Eq. (3.6) for $\alpha = 0.2, a = 2, c = 3, b = 1, a_0 = 0.5, t = 1, z = 1, d = 1$, and $y = 1$.

Family 4: Using $\gamma = \{-1,1,1,1\}, \lambda = \{1,-1,1,-1\}$, then Eq. (2.5) turns to

$$\phi(\varsigma) = \frac{-\sinh(\varsigma)}{\cosh(\varsigma)}. \tag{3.7}$$

Case 1: $b_1 = -2a, s = -\frac{16a^2b+br+2c\beta}{d}, a_1 = -2a, \alpha = \frac{a^3k}{b^3}$.
Using the above values with Eq. (3.7) in Eq. (3.2), we have

$$\psi_4(\varsigma) = a_0 + 2a\coth(\varsigma) + 2a\tanh(\varsigma).$$

Therefore, we have

$$Q_4(x,y,z,t) = a_0 - 2a\coth(ct - ax - by - dz) - 2a\tanh(ct - ax - by - dz). \tag{3.8}$$

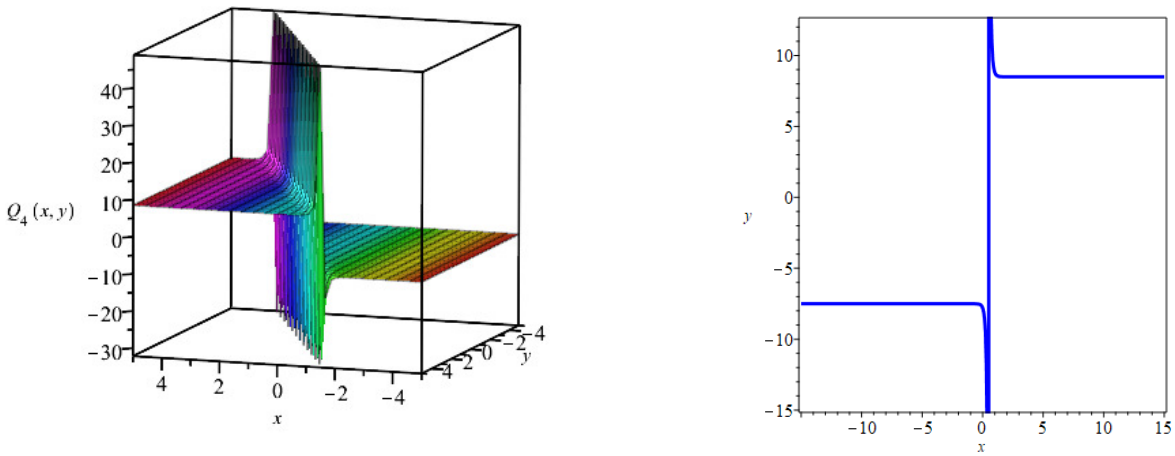

Figure 3.4: 3D dimensional surface and 2D graphs of solution of Eq. (3.8) for the values of $\alpha = 0.2, a = 2, c = 3, b = 1, a_0 = 0.5, t = 1, z = 1, d = 1$, and $y = 1$.

Family 5: Using $\gamma = \{i,-i,1,1\}, \lambda = \{i,-i,i,-i\}$ in Eq. (2.5), then we have

$$\phi(\varsigma) = \frac{\sin(\varsigma)}{\cos(\varsigma)}. \tag{3.9}$$

Case 1: $b_1 = -\frac{2b\alpha^{1/3}}{k^{1/3}}, a = \frac{b\alpha^{1/3}}{k^{1/3}}, \beta = -\frac{br+ds-\frac{16b^3\alpha^{2/3}}{k^{2/3}}}{2c}, a_1 = \frac{2b\alpha^{1/3}}{k^{1/3}}$. Inserting these values with Eq. (3.9) in Eq. (3.2), we have

$$\psi(\varsigma) = a_0 + \frac{2b\alpha^{1/3}\cot(\varsigma)}{k^{1/3}} - \frac{2b\alpha^{1/3}\tan(\varsigma)}{k^{1/3}}.$$

So, we have

$$Q_5(x,y,z,t) = a_0 - \frac{2b\alpha^{1/3}\cot\left(ct-by-dz-\frac{bx\alpha^{1/3}}{k^{1/3}}\right)}{k^{1/3}} + \frac{2b\alpha^{1/3}\tan\left(ct-by-dz-\frac{bx\alpha^{1/3}}{k^{1/3}}\right)}{k^{1/3}}. \tag{3.10}$$

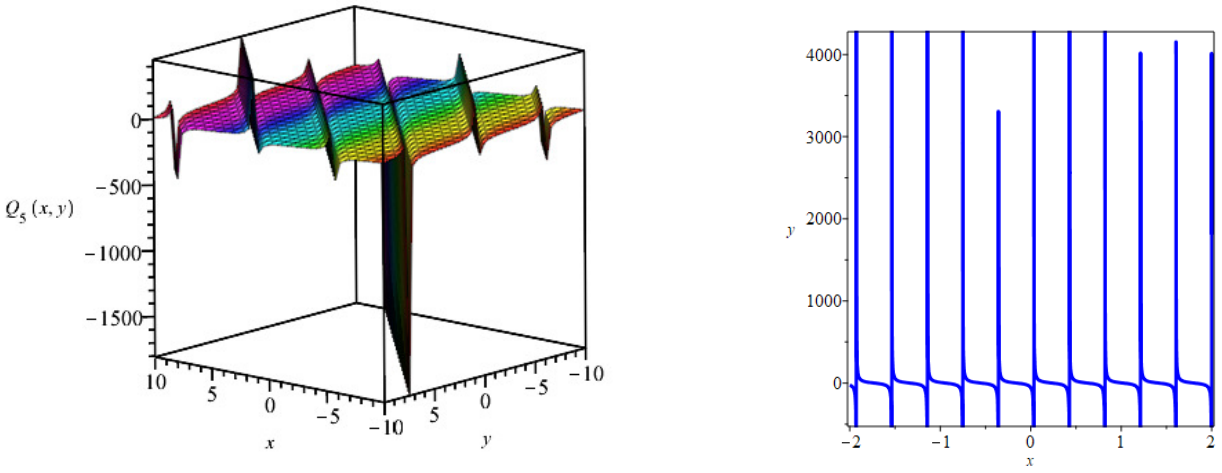

Figure 3.5: 3D dimensional surface and 2D graphs of solution of Eq. (3.10) where $\alpha = 8, a = 2, c = 3, b = 4, a_0 = 0.5, t = 1, z = 1, d = 2, k = 8$, and $y = 1$.

Family 6: Using $\gamma = \{-1,0,1,1\}, \lambda = \{0,0,0,1\}$, then Eq. (2.5) turns to

$$\phi(\varsigma) = -\frac{1}{1+e^{\varsigma}}. \tag{3.11}$$

Case 1: $b_1 = 0, \alpha = \frac{a^3k}{b^3}, s = -\frac{b\left(a^2+r\right)+2c\beta}{d}, a_1 = 2a$. Inserting the above values with Eq. (3.11) to Eq. (3.2), we have

$$\phi(\varsigma) = a_0 - \frac{2a}{1+e^{\varsigma}}.$$

Therefore,

$$Q_6(x,y,z,t) = a_0 - \frac{2a}{1+e^{-ct+ax+by+dz}}. \tag{3.12}$$

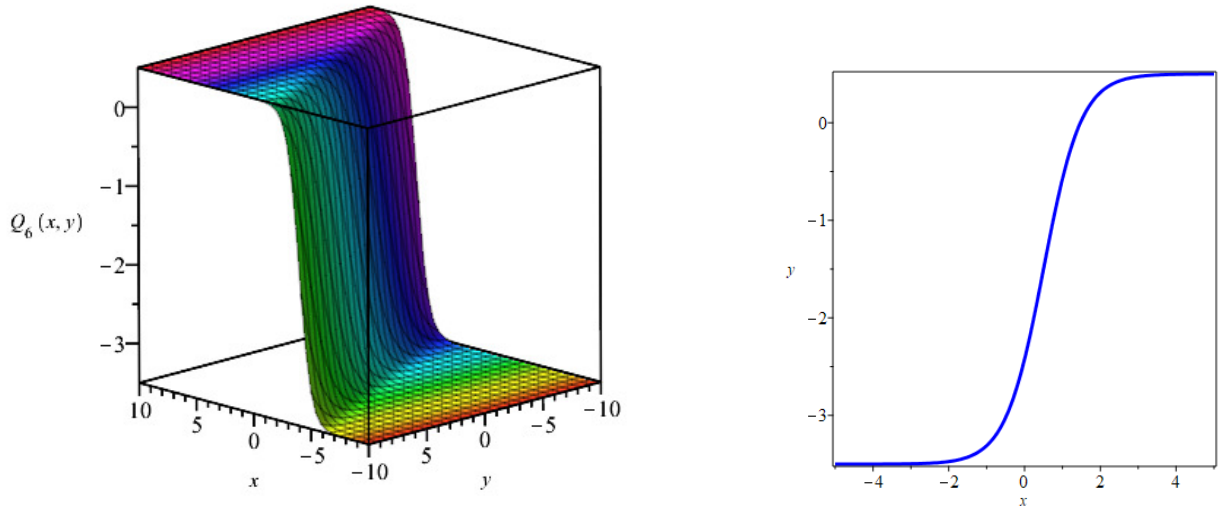

Figure 3.6: 3D dimensional surface and 2D graphs of solution of Eq. (3.12) using $a = 2, c = 3, b = 1, a_0 = 0.5, t = 1, z = 1, d = 1$, and $y = 1$.

Family 7: Using $\gamma = \{1+i, 1-i, 1, 1\}, \lambda = \{i, -i, i, -i\}$ Eq. (2.5) turns to

$$\phi(\varsigma) = \frac{-\sin(\varsigma)+\cos(\varsigma)}{\cos(\varsigma)}. \tag{3.13}$$

Case 1: $b_1 = -\frac{4b\alpha^{1/3}}{k^{1/3}}, a = \frac{b\alpha^{1/3}}{k^{1/3}}, a_1 = 0, s = \frac{br - \frac{4b^3\alpha^{2/3}}{k^{2/3}} + 2c\beta}{d}$. Putting these values with Eq. (3.16) into Eq. (3.3), we have

$$\psi_7(\varsigma) = a_0 - \frac{4b\alpha^{1/3}\cos(\varsigma)}{k^{1/3}(\cos(\varsigma) - \sin(\varsigma))}.$$

So, we have

$$Q_7(x,y,z,t) = a_0 - \frac{4b\alpha^{1/3}\cos\left(ct - by - dz - \frac{bx\alpha^{1/3}}{k^{1/3}}\right)}{k^{1/3}\left(\cos\left(ct - by - dz - \frac{bx\alpha^{1/3}}{k^{1/3}}\right) + \sin\left(ct - by - dz - \frac{bx\alpha^{1/3}}{k^{1/3}}\right)\right)}. \tag{3.14}$$

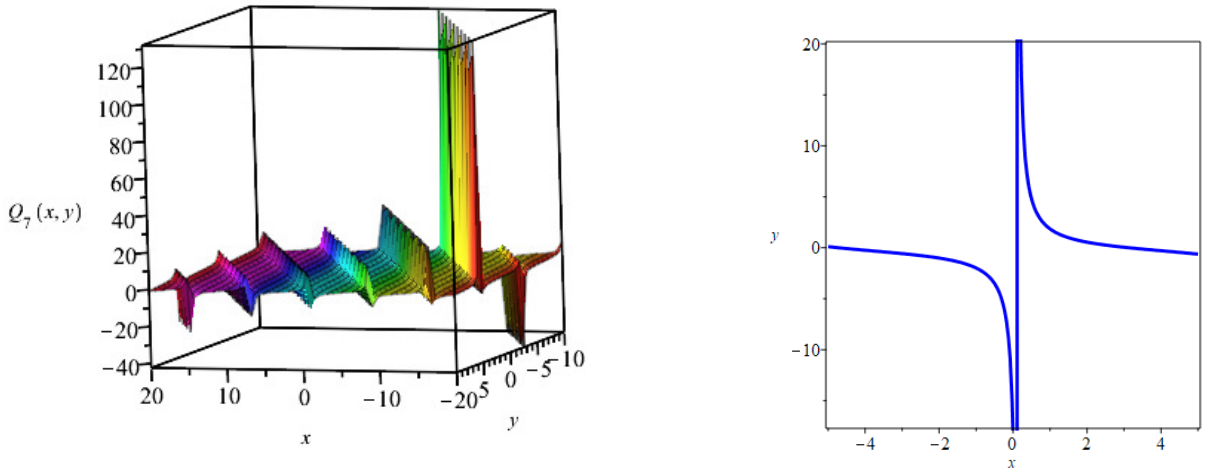

Figure 3.7: : 3D dimensional surface and 2D graphs of solution of Eq. (3.14) using $\alpha = 8, a = 2, c = 3, b = 0.4, a_0 = 0.5, , d = 0.2, k = 8, t = 1, z = 1$, and $y = 1$.

4. Conclusions

In this study, we have investigated the (3+1)-dimensional Date-Jimbo-Kashiwara-Miwa equation via using the generalized exponential rational function method, which is the most power method to study NPDEs. The feature of this method is that we can find abundant different solutions that are dependent on the parameters involved in it. As a result, we constructed some new exact solutions in the type of exponential, trigonometric and hyperbolic solutions. The 3D surfaces and 2D graphs of all obtained solutions are plotted. All constructed solutions satisfy the original equation.

Acknowledgments

The author would like to express their sincere thanks to the editor and the anonymous reviewers for their helpful comments and suggestions.

Funding

There is no funding for this work.

Availability of data and materials

Not applicable.

Competing interests

The author declare that she has no competing interests.

Authors contributions

The author read and approved the final manuscript.

References

[1] S. Kumar, H. Almusawa, I. Hamid, MA Akbar, MA Abdou, *Abundant analytical soliton solutions and Evolutionary behaviors of various wave profiles to the Chaffee–Infante equation with gas diffusion in a homogeneous medium*, Results Phys., (2021), Article ID 104866.

[2] K. K. ALi, R. Yilmazer, H. M. Baskonus, H. Bulut, *Modulation instability analysis and analytical solutions to the system of equations for the ion sound and Langmuir waves*, Phys. Scr., **95** (2020), Article ID 065602.

[3] H. Dutta, H. Günerhan, K. K. Ali, R. Yilmazer, *Exact Soliton Solutions to the Cubic-Quartic Non-linear Schrödinger Equation With Conformable Derivative*, Frontiers in Physics **8** (2020).

[4] W. H. Zhu, L. G. Liu, *Stripe solitons and lump solutions to a generalized (3+ 1)-dimensional B-type Kadomtsev-Petviashvili equation with variable coefficients in fluid dynamics*, J. Math. Anal. Appl., **502** (2021), Article ID 125198.

[5] J. Manafian, O. A. Ilhan, K. K. Ali, S. Abid, *Cross-kink wave solutions and semi-inverse variational method for (3+ 1)-dimensional potential-YTSF equation*, East Asian J. Appl. Math., **10** (2020), 549–65.

[6] H. F. Ismael, H. Bulut, H. M. Baskonus, W. Gao, *Dynamical behaviors to the coupled Schrödinger-Boussinesq system with the beta derivative*, AIMS Math., **6** (2021), 7909–28.

[7] K. K. Ali, R. Yilmazer, H. Bulut, T. Aktürk, M. S. Osman, *Abundant exact solutions to the strain wave equation in micro-structured solids*, Modern Phys. Lett. B, **35** (2021), Article ID 2150439.

[8] H. F. Ismael, A. Seadawy, H. Bulut, *Multiple soliton, fusion, breather, lump, mixed kink-lump and periodic solutions to the extended shallow water wave model in (2+ 1)-dimensions*,Modern Phys. Lett. B, **35** (2021), Article ID 2150138.

[9] J. G. Liu, W. H. Zhu, Y. He, *Variable-coefficient symbolic computation approach for finding multiple rogue wave solutions of nonlinear system with variable coefficients*, Z. Angew. Math. Phys., **72** (2021), 1–12.

[10] W. X. Ma, T. Huang, Y. Zhang, *A multiple exp-function method for nonlinear differential equations and its application*, Phys. Scr., **82** (2010), Article ID 65003.

[11] H. M. Baskonus, *New acoustic wave behaviors to the Davey–Stewartson equation with power-law nonlinearity arising in fluid dynamics*, Nonlinear Dynam., (2016).

[12] Y. X. Li, E. Celik, J. L. Guirao, T. Saeed, H. M. Baskonus, *On the modulation instability analysis and deeper properties of the cubic nonlinear Schrödinger's equation with repulsive δ-potential*, Results Phys., **25** (2021)., Aertcle ID 104303.

[13] S. T. Demiray, H. Bulut, E. Celik, *Soliton solutions of Wu-Zhang system by generalized Kudryashov method*, AIP Conference Proceedings (2037), (2018), (020025).

[14] H. F. Ismael, H. Bulut, H. M. Baskonus, *Optical soliton solutions to the Fokas–Lenells equation via sine-Gordon expansion method and $(m+(G'/G))$-expansion method*, Pramana, **94** (2020), 1–9.

[15] E. Celik, H. Bulut, H. M. Baskonus, *Novel features of the nonlinear model arising in nano-ionic currents throughout microtubules*, Indian J. Phys., **92** (2018), 1137-1143.

[16] J.P. Fang, Q.B. Ren, C.L. Zheng, *New exact solutions and fractal localized structures for the (2+1)-dimensional Boiti–Leon–Pempinelli system*. Z. Naturforsch, **60** (2005), 245–251 .

[17] M. A. Dokuyucu, E. Celik, *Analyzing a novel coronavirus model (COVID-19) in the sense of caputo-fabrizio fractional operator*. Comput. Appl. Math., (2021), 49-69.

[18] H.F. Ismael, M. A. S. Murad, H. Bulut, *Various exact wave solutions for KdV equation with time-variable coefficients*, J. Ocean Eng. Sci., (2021).

[19] H. F. Ismael, H. Bulut, *Nonlinear dynamics of (2+1)-dimensional Bogoyavlenskii-Schieff equation arising in plasma physics*, Math. Methods Appl. Sci., **44**(13) (2021), 10321-10330.

[20] H. F. Ismael, H. Bulut, *Multi soliton solutions, M-lump waves and mixed soliton-lump solutions to the awada-Kotera equation in (2+ 1)-dimensions*, Chinese J. Phys., **71** (2021), 54–61.

[21] F. Dusunceli, E. Celik, M. Askin, H. Bulut, *New exact solutions for the doubly dispersive equation using the improved Bernoulli sub-equation function method*, Indian J. Phys., **95** (2021) 309-314.

[22] X. Guan, W. Liu, Q. Zhou, A. Biswas, *Darboux transformation and analytic solutions for a generalized super-NLS-mKdV equation*, Nonlinear Dyn., **98** (2019), 1491–1500.

[23] K. K. Ali, R. Yilmazer, M. S. Osman, *Extended Calogero-Bogoyavlenskii-Schff equation and its dynamical behaviors*, Phys Scr., (2021).

[24] E. Date, M. Jimbo, M. Kashiwara, T. Miwa, *Transformation groups for soliton equations: IV. A new hierarchy of soliton equations of KP-type*, Phys. D., **4** (1982), 343–65.

[25] A. M. Wazwaz, *A (2+ 1)-dimensional time-dependent Date–Jimbo–Kashiwara–Miwa equation: Painlevé integrability and multiple soliton solutions*, Comput. Math. Appl., **79** (2020), 1145–9.

[26] H. F. Ismael, A. Seadawy, H. Bulut, *Rational solutions, and the interaction solutions to the (2+ 1)-dimensional time-dependent Date–Jimbo–Kashiwara–Miwa equation*, Int. J. Comput. Math., **98**12 (2021), 2369–2377.

[27] A. W. Wazwaz, *New (3+ 1)-dimensional Date-Jimbo-Kashiwara-Miwa equations with constant and time-dependent coefficients: Painlevé integrability*, Phys. Lett. A, **384** (2020), 126787.

[28] H. Almusawa, K. K. Ali, A. M. Wazwaz, M. S. Mehanna, D. Baleanu , M.S. Osman, *Protracted study on a real physical phenomenon generated by media inhomogeneities*, Results Phys., **31** (2021), Article ID 104933.

[29] B. Ghanbari, C. K. Kuo, *New exact wave solutions of the variable-coefficient (1+ 1)-dimensional Benjamin-Bona-Mahony and (2+ 1)-dimensional asymmetric Nizhnik-Novikov-Veselov equations via the generalized exponential rational function method*, Eur. Phys. J. Plus, **134** (2019), 1–13.

[30] B. Ghanbari, *Abundant soliton solutions for the Hirota–Maccari equation via the generalized exponential rational function method*, Modern Phys. Lett. B, **33**(9) (2019), 1950106.

[31] B. Ghanbari, M. Inc, *A new generalized exponential rational function method to find exact special solutions for the resonance nonlinear Schrödinger equation* Eur. Phys. J. Plus, **133**(4) (2018).

[32] K. K. Ali, H. Dutta, R. Yilmazer, S. Noeiaghdam, *On the new wave behaviors of the Gilson-Pickering equation*, Front Phys., **8**(2020).

Journal of Mathematical Sciences and Modelling, 4 (3) (2021) 133-138
Research Article

Journal of Mathematical Sciences and Modelling

Journal Homepage: www.dergipark.gov.tr/jmsm
ISSN 2636-8692
DOI: http://dx.doi.org/10.33187/jmsm.1009561

Stability of an SIRS Epidemic Model with Saturated Incidence Rate and Saturated Treatment Function

İrem Çay[1]

[1]*Department of Mathematics, Faculty of Science and Arts, Kocaeli University, Kocaeli, Turkey*

Article Info

Keywords: *Global stability, Lyapunov function, SIRS epidemic model.*
2010 AMS: *34D20, 34D23*
Received: *14 Octobrt 2021*
Accepted: *22 December 2021*
Available online: *29 December 2021*

Abstract

In this paper the global dynamics of susceptible-infected-recovered-susceptible (SIRS) epidemic model with saturated incidence rate and saturated treatment function is studied. Firstly, the basic reproduction number R_0 is calculated and the existence of the disease-free and positive equilibria is showed. In addition, local stability of the equilibria is investigated. Then, sufficient conditions are achieved for global stability of disease-free and endemic equilibria. Finally, the numerical examples are presented to validate the theoretical results.

1. Introduction

In epidemiology, mathematical modeling is an important tool for observing the dynamic evolution and effects of infectious disease [1]. Using mathematical models, researchers can identify trends in disease, analyze epidemiological studies, and make general predictions about disease. For this purpose, stability and bifurcation analysis of many SIRS epidemic models have been investigated in [2]-[6]. The total population consists of three subpopulations based on disease status in classical infectious disease models: S(t)-susceptible population, I(t)-infective population and R(t)-recovered population, at any given time t. The classic SIRS epidemic model, assuming that the recovering population has transient immunity, can be given as

$$\begin{aligned} \frac{dS}{dt} &= A-\rho S-f(I)S+\delta R, \\ \frac{dI}{dt} &= f(I)S-(\rho+\gamma)I-T(I), \\ \frac{dR}{dt} &= \gamma I-(\rho+\delta)R+T(I). \end{aligned}$$

where the parameter A denotes the natality of susceptible population, ρ is the mortality rate and δ shows the rate of loss of immunity and return to the susceptible class of recovered individuals. γ is the recovery rate of the infected population. $f(I)S$ denotes the incidence rate, and the $f(I)$ function measures the infectious strength of the disease.
In this study, we take a saturated incidence rate

$$f(I)=\frac{\beta I}{1+\alpha I},$$

which firstly presented by Capasso and Serio in [2]. Here, βI calculates the infectious strength of the disease and $\frac{1}{1+\alpha I}$ calculates the inhibitory effect from behavioral change or crowding of infective individuals when the number of susceptible individuals increases.
In addition, we take saturated treatment function as

$$T(I)=\frac{rI}{1+\varepsilon I},$$

which is continuous and differentiable [3]. Here, $rI>0$ and $\varepsilon\geq 0$. r means the cure rate and ε quantifies the extent of the effect of delaying the infected to cure.

Email addresses and ORCID numbers: irem.atac@kocaeli.edu.tr, 0000-0001-9234-2523

In this paper, we present the SIRS epidemic model with saturated incidence rate and saturated treatment function as follows:

$$\frac{dS}{dt} = A - \frac{\beta SI}{1+\alpha I} - \rho S + \delta R, \tag{1.1}$$

$$\frac{dI}{dt} = \frac{\beta SI}{1+\alpha I} - (\rho+\gamma)I - \frac{rI}{1+\varepsilon I}, \tag{1.2}$$

$$\frac{dR}{dt} = \gamma I - (\rho+\delta)R + \frac{rI}{1+\varepsilon I}. \tag{1.3}$$

The remainder of this article is organized as follows. In Section 2, the local stability of the equilibria is examined. In Section 3, adequate conditions for global stability of equilibria are provided by using Lyapunov functions. In Section 4, to validate our theoretical results, some numerical examples are given.

2. Equilibria and Local Dynamics

We start with investigating the positivity and boundedness properties of solutions for system (1.1)-(1.3), for the purpose of ensuring that the model is biologically well-behaved.

Theorem 2.1. *If the initial conditions are $S(0) \geq 0, I(0) \geq 0, R(0) \geq 0$, the solutions of system (1.1)-(1.3) are nonnegative and bounded for all $t \geq 0$.*

Proof. From the model system (1.1)-(1.3), we have

$$\frac{dS}{dt}|_{S=0} = A + \delta R, \quad \frac{dI}{dt}|_{I=0} = 0, \quad \frac{dR}{dt}|_{R=0} = \gamma I + \frac{rI(t)}{1+\varepsilon I(t)}.$$

It is clear that these ratios are not negative in the bounding planes of the non-negative cone of $\mathbb{R}^3$. Therefore, if we start inside this cone, we will always stay inside this cone in the inward direction of the vector field in all bounding planes. Consequently, all solutions of (1.1)-(1.3) are not negative.
For the proof of boundedness, we denote the total population size as $M = S + I + R$. Adding Eqns. (1.1)-(1.3), we obtain

$$\frac{dM}{dt} = A - \rho M. \tag{2.1}$$

If we solve the Eq. (2.1), we find

$$M(t) = \frac{A}{\rho} - \left(\frac{A}{\rho} - M(t_0)\right) e^{-\rho(t-t_0)}$$

where $M(t_0) > 0$ is an initial condition. Thus,

$$\lim_{t\to\infty} M(t) = \frac{A}{\rho}$$

which shows the conclusion. □

From the above theorem, we obtain the following region:

$$\Gamma = \{(S,I,R) \in \mathbb{R}^3_+ | S + I + R \leq \frac{A}{\rho}, S \geq 0, I \geq 0, R \geq 0\}$$

which is a positively invariant set for Eqns. (1.1)-(1.3).
Since the limit set of Eqns. (1.1)-(1.3) is on the plane $S + I + R = \frac{A}{\rho}$, we can concentrate on the following reduced system:

$$\frac{dI}{dt} = \frac{\beta I}{1+\alpha I}\left(\frac{A}{\rho} - I - R\right) - (\rho+\gamma)I - \frac{rI}{1+\varepsilon I}, \tag{2.2}$$

$$\frac{dR}{dt} = \gamma I - (\rho+\delta)R + \frac{rI}{1+\varepsilon I} \tag{2.3}$$

Clearly,

$$\Lambda = \left\{(I,R) | I \geq 0, R \geq 0, I + R \leq \frac{A}{\rho}\right\}.$$

is the positively invariant set of system (2.2)-(2.3)
To put the model in dimensionless form, we build the following variable change:

$$I' = \frac{\beta}{\rho+\gamma} I, \quad R' = \frac{\beta}{\rho+\gamma} R, \quad t' = (\rho+\gamma)t.$$

To avoid making the mathematical notation look bad, we still indicate (I', R', t') by (I, R, t). Then we get

$$\frac{dI}{dt} = \frac{I}{1+mI}(B-I-R)-I-\frac{pI}{1+qI}, \tag{2.4}$$

$$\frac{dR}{dt} = rI-nR+\frac{pI}{1+qI} \tag{2.5}$$

where $m=\frac{\alpha(\rho+\gamma)}{\beta}$, $B=\frac{\beta A}{\rho(\rho+\gamma)}$, $p=\frac{r}{\rho+\gamma}$, $q=\frac{\varepsilon(\rho+\gamma)}{\beta}$, $r=\frac{\rho}{\rho+\gamma}$, $n=\frac{\rho+\delta}{\rho+\gamma}$. It can be seen that $m,n,p,q,r,B>0$ and the positively invariant set of system (2.4)-(2.5) is

$$\tilde{\Lambda}=\{(I,R)|I\geq 0, R\geq 0, I+R\leq B\}.$$

Clearly, system (2.4)-(2.5) always has a unique disease-free equilibrium $E^0=(I^0,R^0)=(0,0)$. The positive equilibria of system (2.4)-(2.5) can be obtained by solving the following equation

$$f(I)=A_1I^2+B_1I+C_1=0 \tag{2.6}$$

where

$$\begin{aligned} A_1 &= \left(1+m+\frac{r}{n}\right)q, \\ B_1 &= q(1-B)+1+m+\frac{r+p}{n}+pm, \\ C_1 &= (p+1)\left(1-\frac{B}{p+1}\right), \end{aligned}$$

Denote $R_0=\frac{B}{p+1}$.

$$R^*=\frac{1}{n}\left(rI^*+\frac{pI^*}{1+qI^*}\right)$$

where I^* is the positive root of the Eq. (2.6). Therefore, system (2.4)-(2.5) has a unique endemic equilibrium $E^*=(I^*,R^*)$.
The Jacobian matrix corresponding to the model Eqns. (2.4)-(2.5) is as follows:

$$J=\begin{pmatrix} \frac{1}{(1+mI)^2}(B-I-R)-\frac{I}{1+mI}-\frac{p}{(1+qI)^2}-1 & -\frac{I}{1+mI} \\ r+\frac{p}{(1+qI)^2} & -n \end{pmatrix}.$$

Now using the variable matrix J obtained above, we get the local stability of the equilibria.

Theorem 2.2. *(i) If $R_0<1$ the disease free equilibrium E^0 of the system (2.4)-(2.5) is locally asymptotically stable otherwise it is unstable. (ii) If $R_0>1$, $A_2<0$ and $B_2>0$, then the unique endemic equilibrium E^* locally asymptotically stable.*

Proof. (i) The Jacobian matrix corresponding to $E^0=(0,0)$ of Eqns. (2.4)-(2.5) is as follows

$$J^0=\begin{pmatrix} B-p-1 & 0 \\ r+p & -n \end{pmatrix}.$$

The eigenvalues of J^0 are

$$\lambda_1=-n,\ \ \lambda_2=B-p-1.$$

Obviously, $\lambda_1<0$. Note that if $R_0<1$, $\lambda_2<0$ and so the disease-free equilibrium E^0 is locally asymptotically stable. Conversely, if $R_0>1$, $\lambda_2>0$ and so E^0 is unstable.
(ii) The Jacobian matrix corresponding to $E^*=(I^*,R^*)$ of Eqns. (2.4)-(2.5) is as follows

$$J^*=\begin{pmatrix} \frac{1}{(1+mI^*)^2}(B-I^*-R^*)-\frac{I^*}{1+mI^*}-\frac{p}{(1+qI^*)^2}-1 & -\frac{I^*}{1+mI^*} \\ r+\frac{p}{(1+qI^*)^2} & -n \end{pmatrix}.$$

The roots of the equation

$$\lambda^2+A_2\lambda+B_2=0$$

are the eigenvalues of J^*. Here

$$\begin{aligned} A_2 &= n+1+\frac{p}{(1+qI^*)^2}+\frac{I^*}{1+mI^*}+\frac{1}{(1+mI^*)^2}(I^*+R^*-B), \\ B_2 &= n\left(1+\frac{p}{(1+qI^*)^2}+\frac{I^*}{1+mI^*}+\frac{1}{(1+mI^*)^2}(I^*+R^*-B)\right) \\ &+ \left(r+\frac{p}{(1+qI^*)^2}\right)\left(\frac{I^*}{1+mI^*}\right). \end{aligned}$$

If $A_2<0$ and $B_2>0$, the eigenvalues of J^* are negative. Thus, proof is completed. □

3. Global Stability

In this chapter, we have obtained the sufficient conditions for global stability for E^0 and E^*.

Theorem 3.1. *If $R_0 < 1$, the disease-free equilibrium $E^0 = (0,0)$ of Eqns. (2.4)-(2.5) is globally asymptotically stable provided that the following condition holds:*

$$Bq < (p+1)m.$$

Proof. Now we will construct a Lyapunov function and use the direct method of Lyapunov to prove the global stability of E^0. Take into the following Lyapunov function

$$V_0(I,R) = I.$$

Clearly V_0 is a positive definite function. If we differentiate V_0 with respect to t, we get

$$\begin{aligned}
\frac{dV_0}{dt} &= \frac{dI}{dt} \\
&= \frac{I}{1+mI}(B-I-R) - I - \frac{pI}{1+qI} \\
&\leq \frac{BI}{1+mI} - \frac{(p+1)I}{1+qI} - \frac{qI^2}{1+qI} \\
&\leq \frac{B-(p+1)}{(1+qI)(1+mI)}I + \frac{Bq-(p+1)m}{(1+qI)(1+mI)}I^2
\end{aligned}$$

Obviously, if $R_0 < 1$ and $Bq < (p+1)m$, then $\frac{dV_0}{dt} \leq 0$. Furthermore, $\frac{dV_0}{dt} = 0$ if and only if $I = 0$. According to LaSalle's principle of invariance [5], this means that all solutions in $\tilde{\Lambda}$ approach the plane $I = 0$ and $R = 0$ as $t \to \infty$. Therefore, we conclude that E^0 is globally asymptotically stable in $\tilde{\Lambda}$. □

Theorem 3.2. *If $R_0 > 1$, then the infected equilibrium $E^* = (I^*, R^*)$ is globally asymptotically stable supplied that the following condition holds:*

$$z_{11} < 0.$$

Proof. To verify the global asymptotic stability of E^*, we apply the method of Lyapunov functions integrated with the Volterra-Lyapunov stable matrices theory [5, 7]. For this, we determine the Lyapunov function as follows:

$$V^* = w_1(I-I^*)^2 + w_2(R-R^*)^2,$$

where w_1, w_2 are positive constants. If we differentiate V^* with respect to time, we get

$$\begin{aligned}
\frac{dV^*}{dt} &= 2w_1(I-I^*)\frac{dI}{dt} + 2w_2(R-R^*)\frac{dR}{dt} \\
&= 2w_1\left(\frac{I}{1+mI}(B-I-R) - \frac{I^*}{1+mI^*}(B-I^*-R^*) - (I-I^*) - \frac{pI}{1+qI} + \frac{pI}{1+qI}\right)(I-I^*) \\
&+ 2w_2\left(r(I-I^*) - n(R-R^*) + \frac{pI}{1+qI} - \frac{pI}{1+qI}\right)(R-R^*) \\
&= 2w_1\left(\frac{B-I-R-(1+mI)I^*}{(1+mI)(1+mI^*)} - \frac{p}{(1+qI)(1+qI^*)}\right)(I-I^*)^2 \\
&- 2w_1\frac{I^*}{(1+mI^*)}(I-I^*)(R-R^*) + 2w_2\left(r + \frac{p}{(1+qI)(1+qI^*)}\right)(I-I^*)(R-R^*) \\
&- 2w_2 n(R-R^*)^2 \\
&= Y(WZ + Z^TW^T)Y^T.
\end{aligned}$$

Here, $Y = (I-I^*, R-R^*)$, $W = diag(w_1, w_2)$ and

$$Z = \begin{pmatrix} z_{11} & z_{12} \\ z_{21} & z_{22} \end{pmatrix},$$

where

$$\begin{aligned}
z_{11} &= \frac{B-I-R-(1+mI)I^*}{(1+mI)(1+mI^*)} - \frac{p}{(1+qI)(1+qI^*)} \\
z_{12} &= -\frac{I^*}{1+mI^*} \\
z_{21} &= r + \frac{p}{(1+qI)(1+qI^*)} \\
z_{22} &= -n
\end{aligned}$$

It is clear that $z_{12} < 0$, $z_{21} > 0$ and $z_{22} < 0$. If $z_{11} < 0$, then Z is Volterra-Lyapunov stable matrix. Therefore, $\frac{dV^*}{dt} < 0$, and by LaSalle's invariance principle [5], E^* is globally asymptotically stable in the interior of $\tilde{\Lambda}$. □

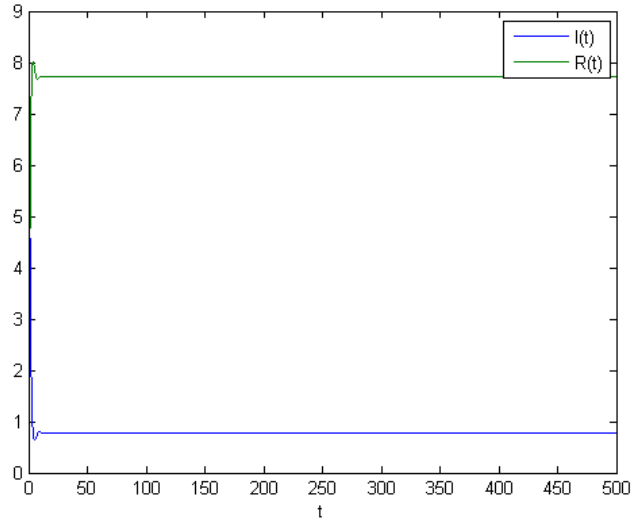

Figure 4.1: The infected equilibrium is $E^* = (I^*, R^*) = (0.7737, 7.7221)$ and it is globally asymptotically stable

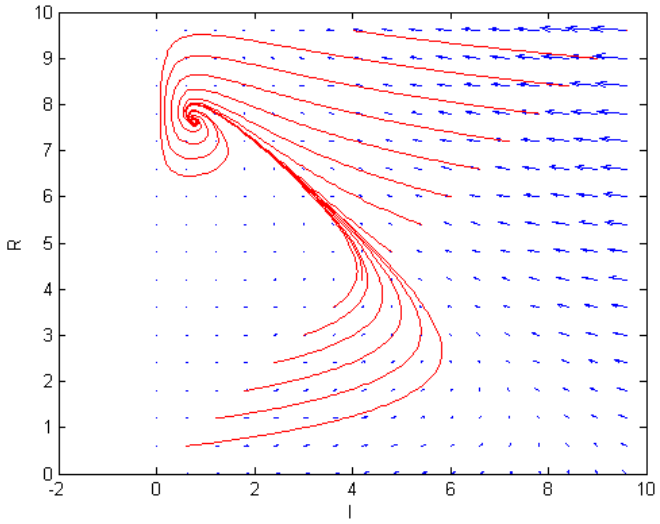

Figure 4.2: When $R_0 > 1$, the phase portrait of Eqns. (2.4)-(2.5) with $E^* = (0.7737, 7.7221)$.

4. Numerical Simulations

We now present some examples to confirm the global stability of the model investigated in Section 3.
Example 4.1: In this example, we set the hypothetical initial values as $(I(0), R(0)) = (5, 1)$. We also take the parameter values as $m = 0.005$, $n = 0.1$, $B = 1$, $p = 0.5$, $q = 0.005$, $r = 0.5$. Thus, $R_0 > 1$ and the infected equilibrium is $E^* = (I^*, R^*) = (0.7737, 7.7221)$. Therefore $E^* = (I^*, R^*) = (0.7737, 7.7221)$ is globally asymptotically stable (See Fig. 4.1 and Fig. 4.2).
Example 4.2: In this example, we set the hypothetical initial values as $(I(0), R(0)) = (5, 1)$. We also take the parameter values as $m = 0.005$, $n = 0.1$, $B = 10$, $p = 0.5$, $q = 0.004$, $r = 0.5$. Thus, $R_0 < 1$ and the disease-free equilibrium $E^0 = (0, 0)$ is globally asymptotically stable (See Fig. 4.3).

5. Conclusion

In this paper, the local and global stability of a SIRS epidemic model with a saturated incidence ratio and a saturated treatment function has been investigated. The basic reproduction number R_0 has been obtained for this model. Next, when $R_0 < 1$ it has been shown that the disease-free equilibrium is globally asymptotically stable , and the infected equilibrium is globally asymptotically stable when $R_0 > 1$. This means that if $R_0 < 1$, the disease has disappeared, otherwise the disease becomes endemic. In this context, we can say that our theoretical results are confirmed by numerical results.

Acknowledgements

The author would like to express their sincere thanks to the editor and the anonymous reviewers for their helpful comments and suggestions.

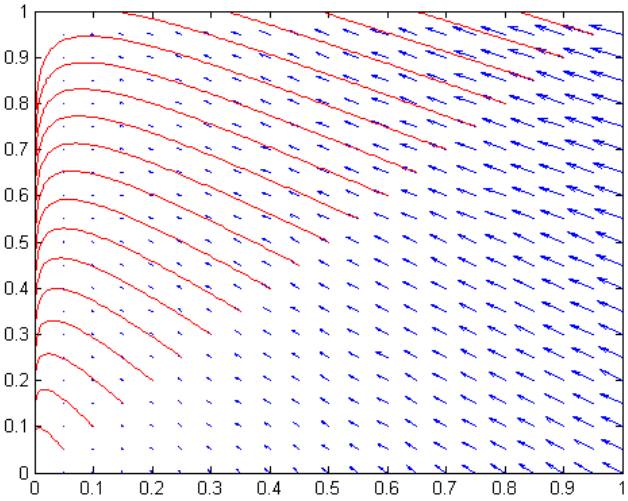

Figure 4.3: When $R_0 < 1$, the phase portrait of Eqns. (2.4)-(2.5) with $E^0 = (0,0)$.

References

[1] F. Brauer, C. Castillo-Chavez, *Mathematical Models in Population Biology and Epidemiology*, Berlin, Springer, 2011.
[2] V. Capasso, G. Serio, *A generalization of the Kermack–Mckendrick deterministic epidemic model*, Math. Biosci. **42** (1978), 43-61.
[3] X. Zhang, X. N. Liu, *Backward bifurcation of an epidemic model with saturated treatment function*, J. Math. Anal. Appl. **348**(1) (2008), 433–443.
[4] E. J. Avila-Vales, A. G. Cervantes-Pérez, *Global Stability for SIRS Epidemic Models with General Incidence Rate and Transfer from Infectious to Susceptible*, SeMA J. Boletín de la Sociedad Matemática Mexicana. **25** (2019), 637–658.
[5] JP. LaSalle, *The Stability of Dynamical Systems*, Philadelphia, PA, USA: Soc. Ind. Appl. Math. 1976.
[6] M. Lu, J. Huang, S. Ruan, P. Yu, *Bifurcation Analysis of a SIRS Epidemic Model with a Generalized Nonmonotone and Saturated Incidence Rate*, . J. Differ. Equ. **267** (2019), 1859-1898.
[7] S. Liao, J. Wang, *Global Stability Analysis of Epidemiological Models Based on Volterra Lyapunov Stable Matrices*, Chaos Solitons Fractals. **45** (2012), 966-977.